

Temporal Straightening for Latent Planning

Ying Wang¹, Oumayma Bounou¹, Gaoyue Zhou¹, Randall Balestriero², Tim G. J. Rudner³, Yann LeCun^{1*}, and Mengye Ren^{1*}

¹New York University ²Brown University ³University of Toronto

Correspondence to {yw3076, yann.lecun, mengye}@nyu.edu

<https://agentlearning.ai/temporal-straightening>

Abstract

Learning good representations is essential for latent planning with world models. While pretrained visual encoders produce strong semantic visual features, they are not tailored to planning and contain information irrelevant—or even detrimental—to planning. Inspired by the perceptual straightening hypothesis in human visual processing, we introduce temporal straightening to improve representation learning for latent planning. Using a curvature regularizer that encourages locally straightened latent trajectories, we jointly learn an encoder and a predictor. We show that reducing curvature this way makes the Euclidean distance in latent space a better proxy for the geodesic distance and improves the conditioning of the planning objective. We demonstrate empirically that temporal straightening makes gradient-based planning more stable and yields significantly higher success rates across a suite of goal-reaching tasks.

1 Introduction

Latent world models offer a compelling solution for planning because they introduce abstraction that improves efficiency and generalization (Nguyen and Widrow, 1989; Sutton, 1991; Ha and Schmidhuber, 2018; Hafner et al., 2020, 2021, 2023; Hansen et al., 2022, 2024). They compress high-dimensional observations into compact latent representations, learn predictive dynamics in that latent space, and enable imaginary rollouts for action optimization. Compared to operating directly in pixel or state space, the latent abstraction reduces dimensionality and ignores noise, making dynamics learning easier and more efficient. At test time, planning is typically posed as optimizing an action sequence by rolling the model forward and minimizing a cost function between the goal and the predicted terminal state in the latent space.

In practice, however, optimization in the learned latent space remains challenging. The induced planning objective is typically highly non-convex, potentially causing gradient-based optimizers to struggle. As a

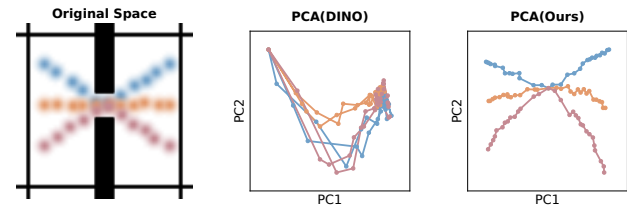


Figure 1: Latent trajectories encoded by a pretrained visual encoder are usually highly curved, increasing the difficulty of prediction and planning. We learn a representation space where feasible trajectories are straighter.

* Equal advising.

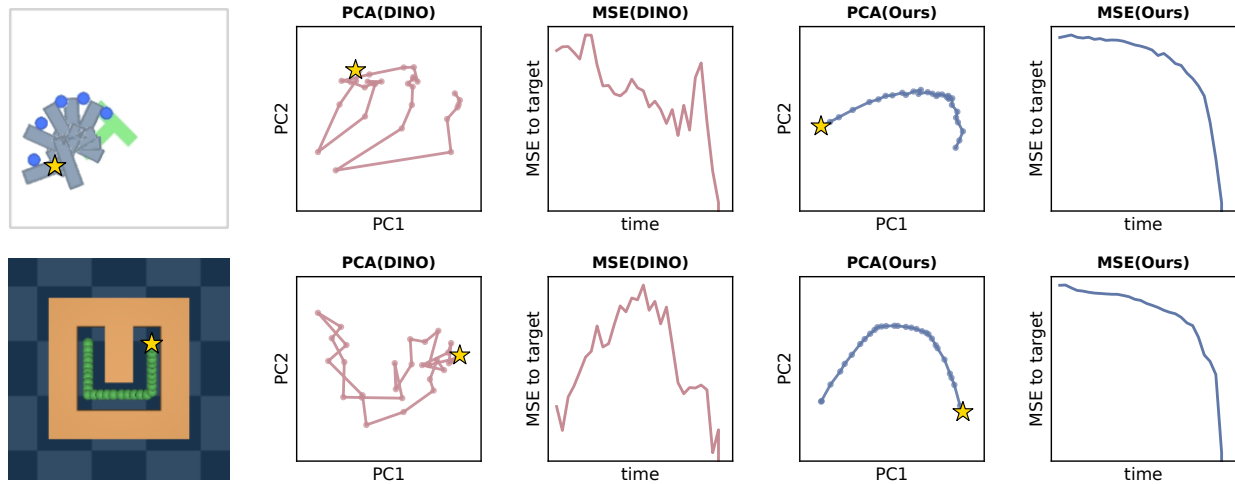


Figure 2: Latent trajectories before vs. after straightening. The upper PushT example is a rotation and the bottom UMaze example shows the agent traveling from the left top to the right top, with the star denoting the target. Straightening yields less curved and smoother trajectories, and makes Euclidean distance a more faithful proxy for geodesic progress towards the goal. More examples are shown in Section D.2.

result, many successful practices (Hafner et al., 2019; Hansen et al., 2024; Zhou et al., 2025; Sobal et al., 2025; Terver et al., 2025) rely on search-based methods such as CEM (Rubinstein, 1997) or MPPI (Williams et al., 2015), which achieve competitive performance but introduce a substantial compute burden and latency. Moreover, commonly used goal cost metrics based on Euclidean distance can be misleading if the embedding space is not properly regularized. In particular, when latent trajectories are highly curved, straight-line distances in embedding space misrepresent the geodesic distance along feasible transitions. These challenges call for better representations that are tailored for latent planning.

What is a “good” representation for latent planning? Large-scale visual pretraining provides powerful semantic-aware features, but it is not tailored to the dynamics of the environments and often retains plenty of planning-irrelevant low-level details. We argue that planning could benefit from representations that are (i) sufficient for predicting dynamics but without task-irrelevant information and (ii) properly regularized so that embedding distances reflect the geodesic distance and gradient-based optimization is reliable. With such representations, we can exploit the differentiability of latent world models and enable efficient gradient-based planning, bypassing the need for computationally expensive search-based methods.

Inspired by the perceptual straightening hypothesis in human vision (Hénaff et al., 2019), which posits that visual systems transform complex videos into straighter internal representations, we introduce a simple approach to straighten latent trajectories for planning. Concretely, we jointly learn an encoder and a predictor of a world model, while imposing regularization on the curvature of latent trajectories during training. The resulting encoded trajectories are significantly straighter, with Euclidean distances better aligned with geodesic distances (Figure 2). We prove that reducing curvature improves convergence of gradient-based planners, and observe superior empirical gains across a suite of goal-reaching tasks: open-loop planning success improves by 20–60% and MPC by 20–30% with a simple gradient-based planner.

2 Related Work

While early visual world models directly predict in pixel spaces and use generated images for control (Oh et al., 2015; Finn and Levine, 2017; Ebert et al., 2018; Du et al., 2023), an increasing number of recent works

first encode high-dimensional sensory inputs into compact latent representations and plan in the resulting latent space. Learning representations is central to these latent world models.

To obtain meaningful representations for world modeling, prior methods add reconstruction-based objectives when training the encoder along with the predictor (Watter *et al.*, 2015; Zhang *et al.*, 2019; Levine *et al.*, 2020; Ha and Schmidhuber, 2018; Hafner *et al.*, 2019, 2020; Micheli *et al.*, 2023; Robine *et al.*, 2023). However, these reconstruction objectives overemphasize low-level visual details that are unnecessary for planning and may fail to capture task-relevant information. More recent approaches decouple perception from dynamics by leveraging strong pretrained visual encoders (Nair *et al.*, 2022; Zhou *et al.*, 2025; Bar *et al.*, 2025; Goswami *et al.*, 2025; Bai *et al.*, 2025; Assran *et al.*, 2025). Closest to our setup, DINO-WM (Zhou *et al.*, 2025) trains task-agnostic predictors and plans directly in frozen DINOv2 (Oquab *et al.*, 2024) feature space. While DINOv2 features provide high-quality visual representations, they are not optimized for planning and may lead to planning objectives that are challenging to optimize. In this work, we improve the representation space for planning by introducing a straightening regularization during world model training.

Joint-Embedding Predictive Architecture (JEPA) emerges as a promising paradigm for world models by learning representations through prediction (LeCun, 2022; Bardes *et al.*, 2024; Assran *et al.*, 2025). It aims to capture predictable structure without retaining unpredictable low-level details, making it more effective and efficient than reconstruction-based objectives (Assel *et al.*, 2025). This paradigm has been shown to be effective for predictive modeling and planning, with training from scratch on offline simulator data (Sobal *et al.*, 2025) and large-scale real-world video pretraining followed by action-conditioned post-training for robotic planning (Assran *et al.*, 2025). Our work also belongs to the JEPA family and focuses on learning better representations.

Temporal Contrastive Learning (Sermanet *et al.*, 2018; Dave *et al.*, 2022; Eysenbach *et al.*, 2024; Yang and Ren, 2025) is also a popular paradigm for learning representations that can reflect the temporal relationships. It encourages temporally close frames to have similar embeddings while distant frames have more dissimilar embeddings through InfoNCE loss (Radford *et al.*, 2021). However, how to choose positive and negative samples requires careful tuning and this objective might push away geodesically close states if suboptimal trajectories are used. Instead, our regularization-based method doesn't require negatives and applies *local* straightening without requiring expert trajectories.

Motivated by the perceptual straightening hypothesis in human vision (Hénaff *et al.*, 2019), some prior works have examined implicit straightening in pretrained visual encoders (Harrington *et al.*, 2023; Internò *et al.*, 2025) or used it as an objective to obtain robust video models (Niu *et al.*, 2024; Bagad and Zisserman, 2025). Implicit straightening is also observed in autoregressive language models optimized for next-word prediction (Hosseini and Fedorenko, 2023; Hosseini *et al.*, 2026). To the best of our knowledge, however, none of these prior works have studied the impact of straightening on planning.

3 Temporal Straightening

We consider control tasks with high-dimensional observations $o_t \in \mathbb{R}^{n_o}$ of an agent interacting with its environment using actions $a_t \in \mathbb{R}^{n_a}$. Our goal is to learn a world model that maps observations to a latent space and models the dynamics in this space, which we use for latent planning.

In this section, we first outline the architecture of our world model, then define the training objectives with a novel geometric regularization that straightens latent trajectories.

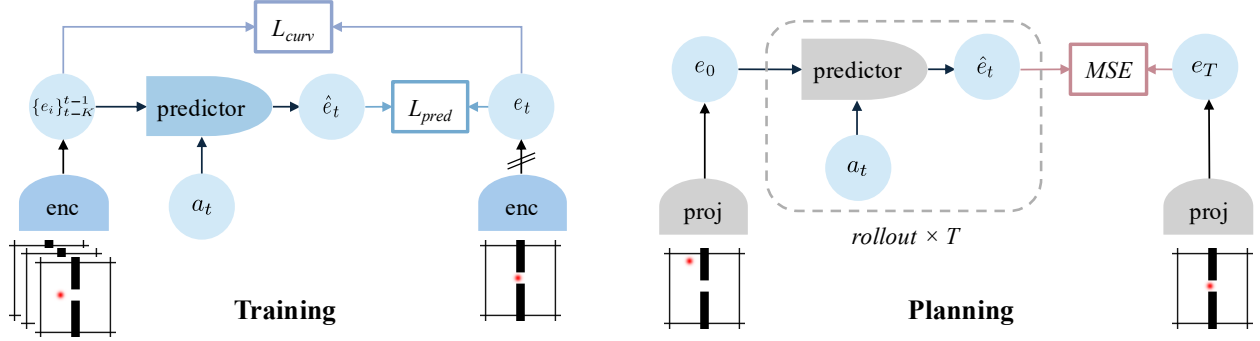


Figure 3: Illustration of Training and Planning. During training, we minimize the prediction loss between the predicted embedding \hat{z}_t^t and the target z_t^t with stop-grad in the target branch, and minimize the local curvature of embeddings. During planning, we rollout for the horizon T using the trained predictor and select optimal actions that minimize the cost between the predicted terminal state and the target in the embedding space.

3.1 World model

Our world model predicts future states in a learned latent space and consists of three components: a sensory encoder, an action encoder, and a predictor.

Sensory encoder. The sensory encoder \mathcal{E}_ϕ^s maps raw observations o_t into latent representations

$$z_t \in \mathbb{R}^d = \mathcal{E}_\phi^s(o_t). \quad (1)$$

The sensory encoder can be any function that maps observations to latent representations. For visual observations, the encoder may preserve spatial structure or collapse it into a global vector representation.

Action encoder. Each action $a_t \in \mathbb{R}^{n_a}$ is mapped to a latent action embedding via

$$\mathcal{E}_\psi^a : \mathbb{R}^{n_a} \rightarrow \mathbb{R}^{d_a}.$$

Predictor. The predictor $f_\theta : \mathbb{R}^{K \times d} \times \mathbb{R}^{K \times d_a} \rightarrow \mathbb{R}^d$ models transitions in the latent space. Given a history of K past latent states and actions, it predicts the next latent state

$$\hat{z}_t = f_\theta \left(\{z_i\}_{i=t-K}^{t-1}, \{\mathcal{E}_\psi^a(a_i)\}_{i=t-K}^{t-1} \right). \quad (2)$$

3.2 Straightening latent trajectories

We seek to straighten the latent space induced by the sensory encoder \mathcal{E}_ϕ^s by penalizing the curvature along trajectories. Let z_t, z_{t+1} , and z_{t+2} be three consecutive latent representations obtained by encoding observations o_t, o_{t+1} , and o_{t+2} using \mathcal{E}_ϕ^s . We define approximate latent velocity vectors

$$v_t = z_{t+1} - z_t, \quad v_{t+1} = z_{t+2} - z_{t+1}, \quad (3)$$

and seek to minimize the angle between them, or equivalently maximize their cosine similarity

$$\mathcal{C} = \frac{v_t \cdot v_{t+1}}{\|v_t\|_2 \cdot \|v_{t+1}\|_2}. \quad (4)$$

3.3 Training objective.

The parameters ϕ, ψ and θ of the world model components $\mathcal{E}_\phi^s, \mathcal{E}_\psi^a$ and f_θ are trained jointly to minimize prediction error and enforce straightened trajectories.

Prediction objective. We minimize the MSE between the predicted and target latent states \hat{z}_{t+1} and z_{t+1} :

$$\mathcal{L}_{pred} = \|\hat{z}_{t+1} - \text{sg}(z_{t+1})\|_2^2, \quad (5)$$

where sg denotes the stop-gradient operation to prevent collapse of the latent space.

Straightening objective. We minimize trajectory curvatures by minimizing the negative cosine similarity

$$\mathcal{L}_{curv} = 1 - \mathcal{C}. \quad (6)$$

This straightening loss can be applied to any differentiable sensory encoder, either in isolation or jointly with the prediction objective.

Overall objective. The total training objective combines prediction and straightening as

$$\mathcal{L}_{total} = \mathcal{L}_{pred} + \lambda \mathcal{L}_{curv}, \quad (7)$$

where $\lambda \geq 0$ controls the strength of the straightening regularization.

Collapse prevention. Since our encoder is trainable, the model is likely to produce degenerate solutions in which all latent representations collapse to a constant. Common anti-collapse strategies can be regularization-based (Bardes et al., 2022; Zhu et al., 2024; Balestrierio and LeCun, 2025; Kuang et al., 2026), contrastive-based (Chen et al., 2020; He et al., 2020), and stop-gradient-based (Chen and He, 2021; Grill et al., 2020). We adopt stop-gradient due to its simplicity and efficiency as it does not require negative samples or introduce new hyperparameters. We apply a stop-gradient operation to the target latent in the prediction loss (5) to prevent the gradients from \mathcal{L}_{pred} from being backpropagated through the target branch. Although a collapsing solution is still possible in theory, stop-gradient has been shown to be effective in self-supervised vision learning (Chen and He, 2021), and has also proved to be effective in our experiments.

4 Planning with Straightened Dynamics

In this section, we present a theoretical analysis on the effect of straightening in the case of a linear dynamical system and show that straightened latent dynamics lead to better convergence in gradient-based planning.

We consider a goal-reaching task where we optimize an action sequence $\mathbf{a} = (a_0, \dots, a_{K-1}) \in \mathbb{R}^{K \times d_a}$ over a horizon K to reach a target latent goal z_g . For simplicity, we use the mean-squared terminal error,

$$\mathcal{L}(\mathbf{a}) = \|z_K - z_g\|_2^2, \quad z_K = \Phi(\mathbf{a}), \quad (8)$$

where Φ denotes unrolling the learned latent dynamics from a fixed initial state z_0 .

Assumption 4.1 (Linear latent dynamics). *For analysis, we consider linear latent dynamics f*

$$f : (z_t, a_t) \rightarrow Az_t + Ba_t, \quad \text{s.t.} \quad z_{t+1} = Az_t + Ba_t, \quad A \in \mathbb{R}^{d \times d}, \quad B \in \mathbb{R}^{d \times d_a}. \quad (9)$$

We first state results for $d_a = d$ and B invertible; see Remark 4.5 for $d_a < d$.

Definition 4.2 (ε -straight transition). Under the linear dynamics $f : (z_t, a_t) \rightarrow Az_t + Ba_t$, we call f ε -straight if

$$\|A - I\|_2 \leq \varepsilon. \quad (10)$$

The term "straight" reflects that, as ε tends to 0, the dynamics of f approach those of the reference function $g : (z_t, a_t) \rightarrow z_t + Ba_t$, where the state evolves linearly along a straight-line trajectory modified only by the control input. We are primarily interested in this regime where ε is small.

Remark 4.3 (Cosine similarity as a practical proxy). In practice, we regularize temporal straightness using the cosine similarity between consecutive latent velocities (4). Under mild bounded-variation assumptions on velocity magnitudes and smooth actions, a large cosine similarity implies that $(A - I)$ is small along visited velocity directions. Detailed proofs are in Section C.3.

Theorem 4.4 (Conditioning of the planning Hessian). *Under Assumption 4.1 with $d_a = d$ and B invertible, unrolling (9) yields*

$$z_K = A^K z_0 + \sum_{t=0}^{K-1} A^{K-1-t} B a_t,$$

so z_K is affine in \mathbf{a} and the planning Hessian is

$$H := \nabla_{\mathbf{a}}^2 \mathcal{L}(\mathbf{a}) = 2J_{\Phi}^{\top} J_{\Phi} \succeq 0, \quad J_{\Phi} = [A^{K-1}B \quad A^{K-2}B \quad \dots \quad B] \in \mathbb{R}^{d \times Kd}.$$

Let $\mathcal{W}_K := J_{\Phi} J_{\Phi}^{\top} = \sum_{k=0}^{K-1} A^k B B^{\top} (A^{\top})^k$ be the finite-horizon controllability Gramian (Kailath, 1980; Sontag, 1998; Chen, 1999). Then the effective condition number $\kappa_{\text{eff}}(H) := \sigma_{\max}(H) / \sigma_{\min}^+(H)$ satisfies

$$\kappa_{\text{eff}}(H) = \kappa(\mathcal{W}_K) \leq \kappa(B)^2 \frac{\sum_{k=0}^{K-1} \sigma_{\max}(A)^{2k}}{\sum_{k=0}^{K-1} \sigma_{\min}(A)^{2k}} \leq \kappa(B)^2 \kappa(A)^{2(K-1)}, \quad (11)$$

where $\kappa(A) := \sigma_{\max}(A) / \sigma_{\min}(A)$. Moreover, if the transition is ε -straight with $\varepsilon = \|A - I\|_2 < 1$, then

$$\kappa_{\text{eff}}(H) \leq \kappa(B)^2 \left(\frac{1 + \varepsilon}{1 - \varepsilon} \right)^{2(K-1)}. \quad (12)$$

For $\varepsilon \leq \frac{1}{2}$, this gives $\kappa_{\text{eff}}(H) \leq \kappa(B)^2 e^{6\varepsilon K}$.

Proofs are in Section C.2.

Remark 4.5 (Low-dimensional actions). When $d_a < d$, B is not invertible and \mathcal{W}_K (hence H) may be singular outside the controllable subspace. Theorem 4.4 holds on $\mathcal{S}_K = \text{range}(\mathcal{W}_K)$ when κ_{eff} is computed using $\sigma_{\min}^+(\mathcal{W}_K)$; see Section C.2.

Theorem 4.4 shows that ε -straight transitions control the condition number of the planning Hessian: when $\varepsilon = \|A - I\|_2$ is small, the Gramian remains better conditioned, yielding $\kappa_{\text{eff}}(H)$ that grows slowly with the horizon. Since the linear planning objective is quadratic with Hessian $H \succeq 0$, gradient descent converges linearly at a rate controlled by the condition number, so the improved bounds on $\kappa_{\text{eff}}(H)$ translate to faster optimization in practice. For nonlinear predictors $z_{t+1} = f_{\theta}(z_t, a_t)$, analogous guarantees require controlling products of state-dependent Jacobians and higher-order terms, which can be a promising direction for future work.

Empirically, we observe that straightening yields a loss landscape with reduced non-convexity (Figure 4). In the next section, we show that it improves gradient-based planning.

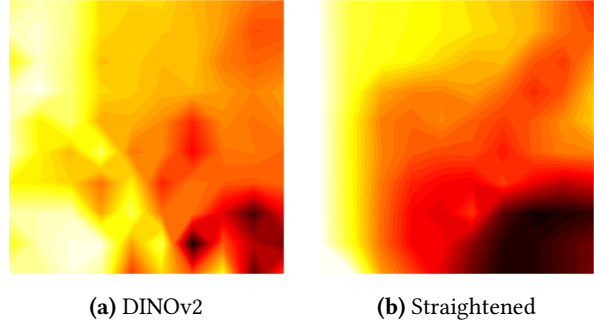


Figure 4: Action-Space Loss Landscape. We pick one test sample from PushT with a planning horizon of 25 steps. For each coordinate (a_x, a_y) in the grid, we fix the first action and optimize the remaining action sequence in the planning horizon to minimize the terminal goal cost. The heatmap represents the minimum attainable loss for each initial action choice, with darker colors indicating lower loss. The loss landscape is closer to convex after straightening.

5 Experiments

To test the effectiveness of the proposed method, we evaluate planning performance on four environments: Wall (Zhou et al., 2025; Sobal et al., 2025), PointMaze UMaze and a more complicated medium-sized maze (Fu et al., 2020), and PushT (Chi et al., 2025). We compare against the baseline DINO-WM (Zhou et al., 2025) which builds on frozen DINOv2 spatial features or CLS tokens. Following DINO-WM’s setup, we use a frameskip of 5 for all environments. Details on the environments and experiments are in Sections A and B.

5.1 Architecture details

Here, we describe the encoder and predictor architectures used to instantiate our world model.

Visual encoder. We consider two encoder setups for the visual encoder \mathcal{E}_ϕ^s :

- A **frozen pretrained** visual backbone with a lightweight projector: We use DINOv2 (Oquab et al., 2024) as the backbone which has shown the best empirical performance for latent planning on 2D navigation tasks (Terver et al., 2025), outperforming DINOv3 (Siméoni et al., 2025) and V-JEPA2 (Assran et al., 2025). Given an observation, the backbone produces spatial features $e_t \in \mathbb{R}^{M \times D}$. We add a trainable lightweight CNN projector \mathcal{P}_ϕ on top of the backbone, leading to

$$z_t^v = \mathcal{P}_\phi(e_t) \in \mathbb{R}^{m_v \times d_v}, \quad (13)$$

where we usually choose $m_v \leq N$ and $d_v \leq D$. The projector may reduce spatial resolution (pooling/striding), channel dimension, or both, encouraging abstraction and reducing computation.

- A ResNet (He et al., 2015) trained **from scratch**, producing features $z_t^v \in \mathbb{R}^{m_v \times d_v}$ directly.

Predictor. We use a ViT (Dosovitskiy et al., 2021) as the dynamics predictor f_θ . When available, proprioceptive states $p_t \in \mathbb{R}^{n_p}$ are encoded via $\mathcal{E}_\xi^p : \mathbb{R}^{n_p} \rightarrow \mathbb{R}^{d_p}$ and concatenated with each visual spatial feature. To condition on actions, we concatenate the action embeddings $z_t^a = \mathcal{E}_\psi^a(a_t) \in \mathbb{R}^{d_a}$ with the visual and proprioceptive embeddings before passing them to the predictor. We apply a temporal causal attention mask so tokens at time t attend only to frames $\{t - K, \dots, t - 1\}$, enabling frame-level autoregressive prediction.

Cosine similarity computation. The straightening loss (Eq. (4)) is only applied on visual latents z_t^v . Different implementations depend on whether latent representations preserve spatial structure:

- **Global features** ($n_v = 1$): Compute the cosine similarity directly between vectors.
- **Spatial features** ($n_v > 1$): We consider four variants: (i) compute the cosine similarity per-patch and average across patches; (ii) flatten all spatial features and then compute the cosine similarity; (iii) average-pool the spatial features before computing the cosine similarity; (iv) use a learnable pooling head to aggregate spatial features before computing the cosine similarity. We use (iv) in the main experiments and ablate these choices in Section B.5.

5.2 How good is the embedding space?

We first inspect the learned embedding space before comparing the downstream planning performance. We measure latent trajectory curvatures and latent Euclidean distances to understand the impact of straightening. For interpretability, we train a VQ-VAE (van den Oord et al., 2017) decoder with a reconstruction loss, detaching latents to stop gradients from the encoder and predictor.

We find that (i) *implicit straightening* can happen when training the encoder using the predictor loss alone; (ii) adding straightening regularization further decreases curvature of the resulting embeddings;

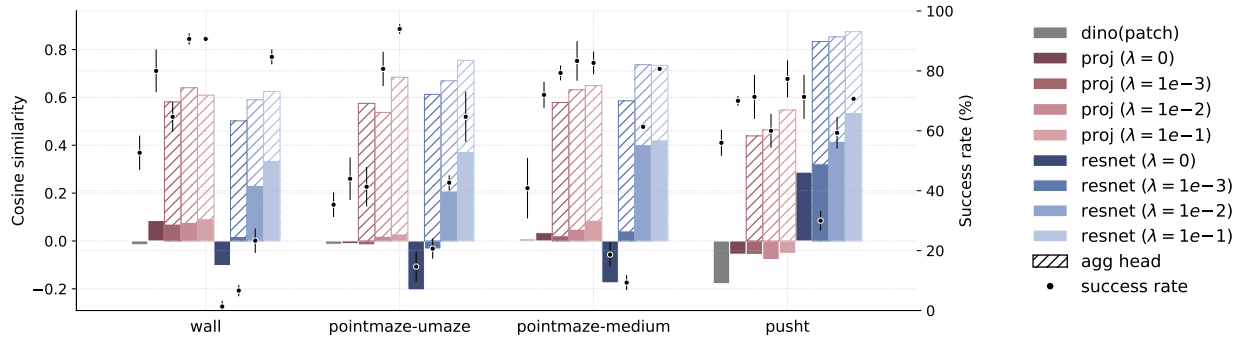


Figure 5: Latent Curvature and Open-Loop GD Success Rate for Different Encoders. Higher cosine similarity indicates lower curvature. Here, we compare models with spatial features and report the average patch-wise cosine similarity. Given the same type of encoder, reduced curvature generally leads to higher success rates.

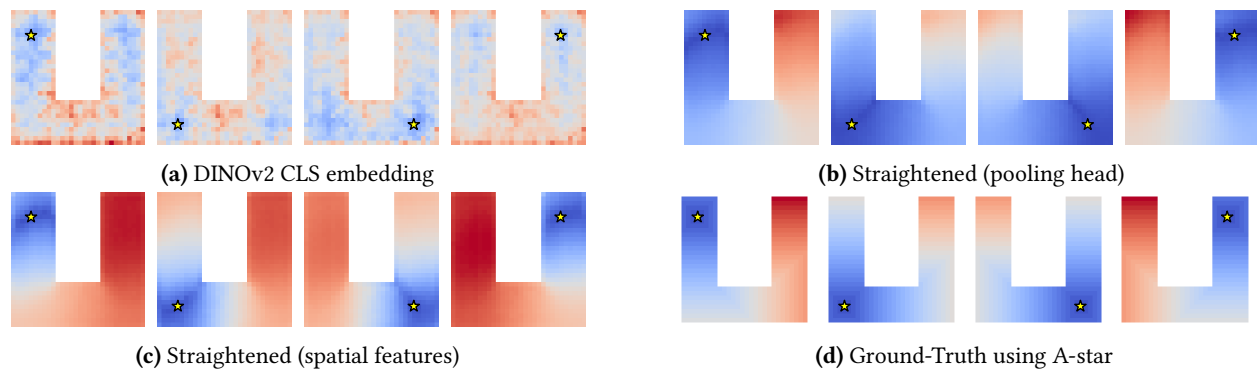


Figure 6: Distance heatmaps of PointMaze (blue indicates small values, and red indicates large values). The yellow star represents the target, and we compute the Euclidean distance between its embedding and those of all other states in the maze. Figures 6b and 6c use ResNet with output features $z \in \mathbb{R}^{14 \times 14 \times 8}$, trained with straightening regularization. After straightening, the latent distance accurately reflects the minimum number of steps required to reach the target.

(iii) straightening encourages the latent Euclidean distance to better align with the geodesic distance; (iv) near-perfect reconstruction can be attained with a very low feature dimensionality.

Reduced curvature. In Figure 5, we compare the curvature of test latent trajectories by computing the cosine similarity of the difference in adjacent frames as in Equation (6). We also visualize the latent trajectories using PCA as shown in Figure 2 and section D.2.

The pretrained DINOv2 embedding space is highly curved as shown in the PCA plots and suggested by the low cosine similarities. The embedding space generally becomes straighter after training even without explicit straightening regularization. We attribute this *implicit straightening* to the JEPa objective: it favors representations whose temporal evolution is easy to predict, so training pressure reduces abrupt directional changes in the latent trajectory. With the *explicit straightening* regularization, the curvature of the embedding space is effectively reduced further. We observe that training a ResNet encoder from scratch generally yields lower curvatures than training a projector on top of a frozen pretrained visual backbone, likely because it offers greater representational flexibility to adapt the geometry to the dynamics.

When straightening is applied on the learnable pooling head, the curvature of the aggregated features is significantly reduced while the underlying spatial features are not forced to be overly straightened. For example, PushT has more complex object motions and the patch-wise cosine similarity is unable to

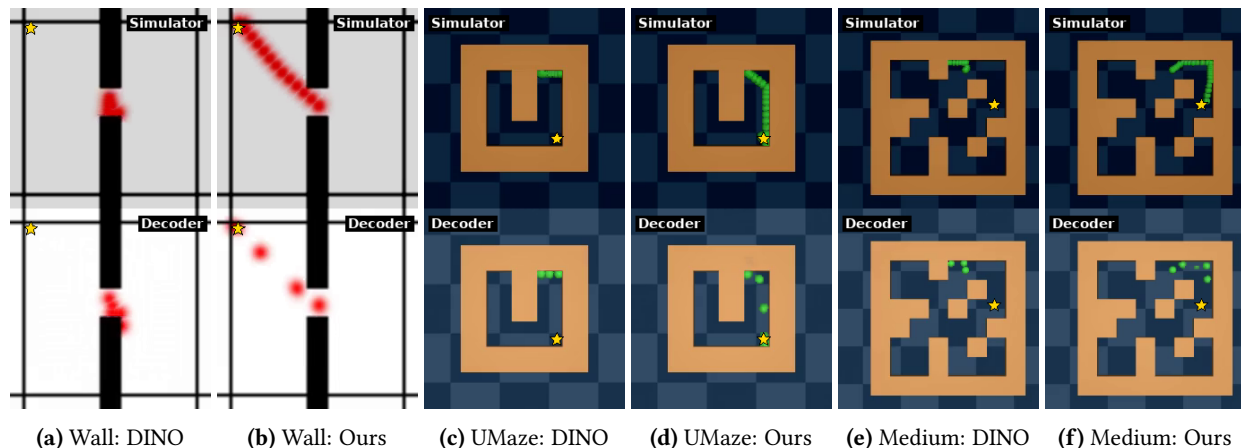


Figure 7: Comparison of Open-loop GD Planning. The star denotes the target. For each subfigure, the upper row shows the overlaid rendered images from the simulator by executing the actions, and the bottom shows imaginary rollouts (with a frameskip of 5) decoded using a trained decoder. GD planners are easily stuck with pretrained DINOv2 features, while straightening significantly improves the success rate. More examples of open-loop planning are in Section D.3.

faithfully capture the global state changes. The introduction of a pooling head increases the flexibility of representation learning and generally leads to better planning performance (Section B.5). We thus use this implementation for the main experiments.

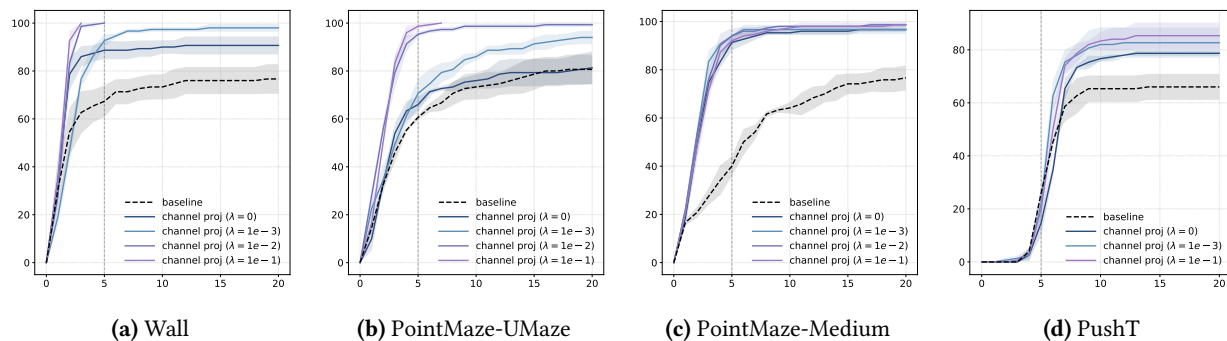
Faithful distance. Although DINOv2 is a strong visual encoder for various downstream vision tasks, it is not optimized for planning and control. As shown in Figure 2, MSE (which is equal to the squared Euclidean distance) between pretrained DINOv2 features does not reflect the progress of moving towards the target. To better understand the limitation of DINOv2, we visualize the Euclidean distance between the embedding of a target state and all other states in the maze in Figure 6. We also compare with ground-truth geodesic distance maps, computed using the A-star search algorithm on the grid of the maze. More heatmaps from different environments and encoders are in Section D.1.

Straightening results in a distance heatmap that closely aligns with the geodesic distance. Notably, the model is only trained on suboptimal, non-expert trajectories. Yet, it does not simply memorize the inefficient paths from the training data; instead, it learns to approximate the minimum number of steps required to transition between states. We also find that the spatial features and aggregated global features capture different levels of distance information. The spatial features preserve local geometry and thus yield fine-grained, locally discriminative distance variations, whereas global features provide a smoother, more coherent long-range signal that better reflects long-horizon distance-to-goal trends.

Sufficient information. To examine whether or not these projected features preserve sufficient information for planning, we train a decoder to reconstruct latents back to images. The decoder is solely for interpretability purposes, and we use stop-gradient to prevent it from affecting the world model. Note that perfect reconstruction is not necessary for planning, since only planning-relevant information must be preserved. However, because these environments are visually simple, even aggressively compressed features reconstruct the observations with high fidelity, as shown in Figure 7. This indicates that the resulting features retain sufficient planning-relevant information.

Table 1: Goal-reaching Success Rate of 50 Test Samples (%) using the GD planner. Values are mean \pm std over three data sampling seeds. The best values are **bold**.

Method	Config		Wall		PointMaze - UMaze		PointMaze - Medium		PushT	
	dim	\mathcal{L}_{curv}	Open-loop	MPC	Open-loop	MPC	Open-loop	MPC	Open-loop	MPC
DINOV2 (CLS)	1×384	\times	28.67 ± 12.68	66.67 ± 10.50	25.33 ± 0.94	82.67 ± 9.98	20.00 ± 8.16	67.50 ± 3.54	19.33 ± 8.22	28.00 ± 1.63
DINOV2 (patch) + proj	1×384	\times	28.67 ± 0.94	76.00 ± 4.90	34.67 ± 1.89	79.33 ± 2.49	18.00 ± 1.63	46.00 ± 3.27	2.00 ± 1.63	11.33 ± 3.40
DINOV2 (patch) + proj	1×384	\checkmark	42.00 ± 3.27	56.67 ± 4.11	38.67 ± 3.40	96.00 ± 0.00	22.67 ± 5.73	78.00 ± 2.83	5.33 ± 3.40	14.67 ± 0.94
ResNet (from scratch)	1×384	\times	4.67 ± 3.40	10.00 ± 1.63	82.00 ± 8.49	96.00 ± 2.83	66.00 ± 2.83	91.33 ± 0.94	2.00 ± 2.83	29.33 ± 3.40
ResNet (from scratch)	1×384	\checkmark	84.00 ± 7.12	100.00 ± 0.00	52.00 ± 6.53	86.67 ± 0.94	54.00 ± 7.12	98.00 ± 0.00	19.33 ± 3.40	48.67 ± 4.99
DINOV2 (patch)	$14 \times 14 \times 384$	\times	52.67 ± 5.73	76.67 ± 6.18	35.33 ± 4.11	80.67 ± 6.18	40.83 ± 10.07	76.67 ± 5.14	56.00 ± 4.32	66.00 ± 4.90
DINOV2 (patch) + proj	$14 \times 14 \times 8$	\times	80.00 ± 7.12	90.67 ± 3.77	44.00 ± 7.12	81.33 ± 6.80	72.00 ± 4.32	96.67 ± 0.94	70.00 ± 1.63	78.67 ± 0.94
DINOV2 (patch) + proj	$14 \times 14 \times 8$	\checkmark	90.67 ± 0.94	100.00 ± 0.00	94.00 ± 1.63	100.00 ± 0.00	82.67 ± 3.77	98.67 ± 0.94	77.33 ± 6.18	85.33 ± 4.99
ResNet (from scratch)	$14 \times 14 \times 8$	\times	1.33 ± 1.89	6.67 ± 1.89	14.67 ± 4.99	66.00 ± 9.09	18.67 ± 4.11	57.33 ± 4.71	71.33 ± 7.36	70.67 ± 10.50
ResNet (from scratch)	$14 \times 14 \times 8$	\checkmark	84.67 ± 2.49	100.00 ± 0.00	64.67 ± 8.38	98.67 ± 1.89	80.67 ± 0.94	99.33 ± 0.94	70.67 ± 0.94	91.33 ± 2.49

**Figure 8:** Success Rate over MPC Steps. The dashed black lines represent DINO-WM with frozen DINOv2 patch features. The solid lines represent frozen DINOv2 patch features with a trainable channel projector (with resulting features $z \in \mathbb{R}^{14 \times 14 \times 8}$) with different strengths of straightening. Our model reaches 100% success rates very quickly as shown in Figures 8a and 8b.

5.3 Planning

We show that straightening can significantly improve the success rates in both open- and closed-loop planning using simple gradient descent on various environments. We also show that retaining the spatial dimensions is more effective than using a global projector, and that increasing channels does not lead to improvement in planning.

Setup. The target states are sampled to guarantee they can be reached within 25 steps from the start states. We follow DINO-WM (Zhou et al., 2025) in using a frameskip of five, so we only need to rollout the world model for $H = 5$ times. During test time, an action sequence is optimized using gradient descent through the learned dynamics model (f_θ) to minimize a goal cost (for comparison with CEM, see Section B.2). For PushT, we assume we have both target images and proprioceptions; for the rest of the environments, we assume we only have target images to increase the difficulty.

We evaluate performance in both open-loop and closed-loop settings. Open-loop planning optimizes a length- H action sequence using the MSE between the terminal embedding and the target embedding as the planning cost. Closed-loop MPC replans at every step: it optimizes a length- H action sequence, executes only the first action, and then replans, using a weighted objective that encourages the predicted trajectory to approach the target (Details are in Section B.1). For PushT specifically, we use only the terminal loss within horizon H because regime-switching dynamics make intermediate-state loss misleading, so we apply the weighted intermediate loss only beyond H where it is more stable.



Figure 9: Examples of Long-Horizon Open-Loop GD Planning on PushT. For each example, the top row shows simulator-rendered images and the bottom row shows decoded images, with the last column being the target. The failure example shows a case where the long-horizon imagined rollout does not match the real dynamics.

Results. As shown in Table 1, we observe a significant improvement across all variants and environments. When training the projectors or encoders, we observe an improvement in performance even without the straightening regularization. We attribute this improvement to the *implicit straightening* during training as discussed in Section 5.2. For ResNet with spatial features, we observe abnormally low success rates for Wall, PointMaze-UMaze and PointMaze-Medium, which could be explained by the extremely high curvature in Figure 5, suggesting a degradation of features. We also notice that the implicit straightening is the weakest for the UMaze when using the projector, which also results in the lowest improvement in planning.

Applying explicit straightening further strengthens the straightness in the embedding space, resulting in more than 10% boost in open-loop and MPC success rates for almost all setups. For example, UMaze’s open-loop success rate is improved from 44% to 94% with the projector, and 14.67% to 64.67% when training a ResNet from scratch. Note that we use weighted loss on intermediate states which enables reaching the target before consuming the full horizon $H = 5$. It is impressive that our model reaches 100% success with MPC on Wall and UMaze within only a few steps (Figure 8), suggesting it discovers more direct trajectories than the randomly generated test trajectories. The PushT success increases more slowly because we apply only the terminal loss within the horizon $H = 5$, yet straightening still yields substantial final gains.

Effect of feature dimensions. We find that preserving spatial structure generally matters more than retaining channels. When we keep all patch tokens, we can aggressively reduce the channel dimension of DINOv2 features from 384 down to 8 without degrading performance. Increasing the channel dimension to $d \in \{32, 128\}$ does not improve performance and can even lead to a drop for some environments (Section B.4), which is not surprising as lower dimensions can simplify both dynamics prediction and downstream optimization. In contrast, collapsing patch features into a single global vector makes precise dynamics prediction harder. The predictor produces less accurate rollouts, which in turn reduces planning success. Notably, training a ResNet from scratch produces significantly better global features than training a global projector applied to frozen DINO patch features.

Long horizon. To further stress test our method, we also evaluate a longer-horizon setting where the target is 50 steps away. We leave out UMaze and Wall, because in those environments a target picked via random 50-step rollouts can even end up surprisingly close in terms of shortest-path distance, making it unable to reflect true long-horizon diffi-

Table 2: Longer-Horizon Success Rate (%).

Model	\mathcal{L}_{curv}	PushT		PointMaze – Medium	
		Open-loop	MPC	Open-loop	MPC
DINO-WM	–	3.33 ± 2.36	27.33 ± 6.66	35.00 ± 2.35	65.33 ± 3.13
+ Channel Proj	✗	6.67 ± 3.77	26.67 ± 9.98	60.00 ± 3.27	72.00 ± 0.00
+ Channel Proj	✓	13.33 ± 3.77	24.00 ± 6.53	68.00 ± 8.64	88.00 ± 3.27
+ ResNet	✗	13.33 ± 3.77	29.33 ± 9.43	14.67 ± 6.80	48.00 ± 9.80
+ ResNet	✓	10.67 ± 4.99	33.33 ± 4.99	76.00 ± 6.53	98.67 ± 1.89

culty. We summarize the results in Table 2 and show success and failure examples in Figure 9. As expected, success rates drop substantially compared to the short-horizon setting, but our method consistently outperforms the baseline across all settings. More broadly, long-horizon rollouts remain a well-known challenge for latent planning where prediction errors compound over steps and lead to substantial trajectory drift. This is visible in failure cases where decoded rollouts become blurry or misaligned with the simulator.

Teleported-PointMaze. DINOv2 embeddings primarily reflect visual similarity, whereas our straightening objective is designed to align the latent space with temporal dynamics. To test whether straightening truly captures dynamics rather than exploiting appearance cues, we introduce *Teleported-PointMaze* with modified transitions: touching the right wall instantly teleports the agent to the left side (Details in Section E). This creates states that look similar (e.g., near walls) but have drastically different temporal distances, so relying on visual similarity alone can be misleading. We visualize a representative success case in Figure 24, where the straightened model plans to reach the target by leveraging teleportation.

6 Conclusion

In this work, we show that temporal straightening yields an embedding space that effectively facilitates latent planning. In this straightened representation space, the Euclidean distance provides a more reliable proxy for the geodesic distance and gradient-based planning is better conditioned. Across a range of 2D goal-reaching tasks, this leads to significant and consistent gains over baselines. More broadly, our findings highlight that representation geometry plays an important role in latent planning and show that straightening latent trajectories is a simple yet effective way to improve it. We believe this opens a promising path toward more efficient latent planning in richer and more challenging environments.

Acknowledgments

We thank Yilun Kuang and Daohan Lu for helpful discussions. This work was supported in part by AFOSR under grant FA95502310139, NSF Award 1922658, Visko AI and the Institute of Information & Communications Technology Planning Evaluation (IITP) under grant RS-2024-00469482, funded by the Ministry of Science and ICT (MSIT) of the Republic of Korea in connection with the Global AI Frontier Lab International Collaborative Research. The compute is supported by the NYU High Performance Computing resources, services, and staff expertise.

References

- Assel, H. V., Ibrahim, M., Biancalani, T., Regev, A., and Balestrero, R. (2025). Joint embedding vs reconstruction: Provable benefits of latent space prediction for self supervised learning. *NeurIPS*.
- Assran, M., Bardes, A., Fan, D., Garrido, Q., Howes, R., Mojtaba, Komeili, Muckley, M., Rizvi, A., Roberts, C., Sinha, K., Zholus, A., Arnaud, S., Gejji, A., Martin, A., Hogan, F. R., Dugas, D., Bojanowski, P., Khalidov, V., Labatut, P., Massa, F., Szafraniec, M., Krishnakumar, K., Li, Y., Ma, X., Chandar, S., Meier, F., LeCun, Y., Rabbat, M., and Ballas, N. (2025). V-jepa 2: Self-supervised video models enable understanding, prediction and planning. *arXiv preprint arXiv:2506.09985*.
- Bagad, P. N. and Zisserman, A. (2025). Chirality in action: Time-aware video representation learning by latent straightening. *NeurIPS*.

- Bai, Y., Tran, D., Bar, A., LeCun, Y., Darrell, T., and Malik, J. (2025). Whole-body conditioned egocentric video prediction. *arXiv preprint arXiv:2506.21552*.
- Balestriero, R. and LeCun, Y. (2025). Lejeba: Provable and scalable self-supervised learning without the heuristics. *arXiv preprint arXiv:2511.08544*.
- Bar, A., Zhou, G., Tran, D., Darrell, T., and LeCun, Y. (2025). Navigation world models. In *CVPR*.
- Bardes, A., Garrido, Q., Ponce, J., Chen, X., Rabbat, M., LeCun, Y., Assran, M., and Ballas, N. (2024). Revisiting feature prediction for learning visual representations from video. *arXiv preprint arXiv:2404.08471*.
- Bardes, A., Ponce, J., and LeCun, Y. (2022). Vicreg: Variance-invariance-covariance regularization for self-supervised learning. *ICLR*.
- Chen, C.-T. (1999). *Linear System Theory and Design*. The Oxford Series in Electrical and Computer Engineering. Oxford University Press, 3 edition.
- Chen, T., Kornblith, S., Norouzi, M., and Hinton, G. (2020). A simple framework for contrastive learning of visual representations. *ICML*.
- Chen, X. and He, K. (2021). Exploring simple siamese representation learning. *CVPR*.
- Chi, C., Xu, Z., Feng, S., Cousineau, E., Du, Y., Burchfiel, B., Tedrake, R., and Song, S. (2025). Diffusion policy: Visuomotor policy learning via action diffusion. *IJRR*.
- Dave, I., Gupta, R., Rizve, M. N., and Shah, M. (2022). Tclr: Temporal contrastive learning for video representation. *Computer Vision and Image Understanding*.
- Dosovitskiy, A., Beyer, L., Kolesnikov, A., Weissenborn, D., Zhai, X., Unterthiner, T., Dehghani, M., Minderer, M., Heigold, G., Gelly, S., Uszkoreit, J., and Houlsby, N. (2021). An image is worth 16x16 words: Transformers for image recognition at scale. *ICLR*.
- Du, Y., Yang, S., Dai, B., Dai, H., Nachum, O., Tenenbaum, J., Schuurmans, D., and Abbeel, P. (2023). Learning universal policies via text-guided video generation. *NeurIPS*.
- Ebert, F., Finn, C., Dasari, S., Xie, A., Lee, A., and Levine, S. (2018). Visual foresight: Model-based deep reinforcement learning for vision-based robotic control. *arXiv preprint arXiv:1812.00568*.
- Eysenbach, B., Myers, V., Salakhutdinov, R., and Levine, S. (2024). Inference via interpolation: Contrastive representations provably enable planning and inference. *NeurIPS*.
- Finn, C. and Levine, S. (2017). Deep visual foresight for planning robot motion. *ICRA*.
- Fu, J., Kumar, A., Nachum, O., Tucker, G., and Levine, S. (2020). D4rl: Datasets for deep data-driven reinforcement learning. *arXiv preprint 2004.07219*.
- Goswami, R. G., Bar, A., Fan, D., Yang, T.-Y., Zhou, G., Krishnamurthy, P., Rabbat, M., Khorrami, F., and LeCun, Y. (2025). World models can leverage human videos for dexterous manipulation. *arXiv preprint arXiv:2512.13644*.
- Grill, J.-B., Strub, F., Altché, F., Tallec, C., Richemond, P. H., Buchatskaya, E., Doersch, C., Pires, B. A., Guo, Z. D., Azar, M. G., Piot, B., Kavukcuoglu, K., Munos, R., and Valko, M. (2020). Bootstrap your own latent: A new approach to self-supervised learning. *NeurIPS*.

- Ha, D. and Schmidhuber, J. (2018). World models. *arXiv preprint arXiv:1803.10122*.
- Hafner, D., Lillicrap, T., Ba, J., and Norouzi, M. (2020). Dream to control: Learning behaviors by latent imagination. *ICLR*.
- Hafner, D., Lillicrap, T., Fischer, I., Villegas, R., Ha, D., Lee, H., and Davidson, J. (2019). Learning latent dynamics for planning from pixels. *ICML*.
- Hafner, D., Lillicrap, T., Norouzi, M., and Ba, J. (2021). Mastering atari with discrete world models. *ICLR*.
- Hafner, D., Pasukonis, J., Ba, J., and Lillicrap, T. (2023). Mastering diverse domains through world models. *arXiv preprint arXiv:2301.04104*.
- Hansen, N., Su, H., and Wang, X. (2024). Td-mpc2: Scalable, robust world models for continuous control. *ICLR*.
- Hansen, N., Wang, X., and Su, H. (2022). Temporal difference learning for model predictive control. *ICML*.
- Harrington, A., DuTell, V., Tewari, A., Hamilton, M., Stent, S., Rosenholtz, R., and Freeman, W. T. (2023). Exploring perceptual straightness in learned visual representations. *ICLR*.
- He, K., Fan, H., Wu, Y., Xie, S., and Girshick, R. (2020). Momentum contrast for unsupervised visual representation learning. *CVPR*.
- He, K., Zhang, X., Ren, S., and Sun, J. (2015). Deep residual learning for image recognition. *CVPR*.
- Hénaff, O. J., Goris, R. L. T., and Simoncelli, E. P. (2019). Perceptual straightening of natural videos. *Nature Neuroscience*.
- Hosseini, E. A. and Fedorenko, E. (2023). Large language models implicitly learn to straighten neural sentence trajectories to construct a predictive representation of natural language.
- Hosseini, E. A., Li, Y., Bahri, Y., Campbell, D., and Lampinen, A. K. (2026). Context structure reshapes the representational geometry of language models. *arXiv preprint arXiv:2601.22364*.
- Internò, C., Geirhos, R., Olhofer, M., Liu, S., Hammer, B., and Klindt, D. (2025). AI-generated video detection via perceptual straightening. *The Thirty-ninth Annual Conference on Neural Information Processing Systems*.
- Kailath, T. (1980). *Linear Systems*. Prentice-Hall.
- Kuang, Y., Dagade, Y., Rudner, T. G., Balestriero, R., and LeCun, Y. (2026). Rectified lpjepa: Joint-embedding predictive architectures with sparse and maximum-entropy representations. *arXiv preprint arXiv:2602.01456*.
- LeCun, Y. (2022). A path towards autonomous machine intelligence version.
- Levine, N., Chow, Y., Shu, R., Li, A., Ghavamzadeh, M., and Bui, H. (2020). Prediction, consistency, curvature: Representation learning for locally-linear control. *ICLR*.
- Micheli, V., Alonso, E., and Fleuret, F. (2023). Transformers are sample-efficient world models. *ICLR*.
- Nair, S., Rajeswaran, A., Kumar, V., Finn, C., and Gupta, A. (2022). R3m: A universal visual representation for robot manipulation. *CoRL*.

- Nguyen, D. and Widrow, B. (1989). The truck backer-upper: an example of self-learning in neural networks. *IJCNN*.
- Niu, X., Savin, C., and Simoncelli, E. P. (2024). Learning predictable and robust neural representations by straightening image sequences. *NeurIPS*.
- Oh, J., Guo, X., Lee, H., Lewis, R., and Singh, S. (2015). Action-conditional video prediction using deep networks in atari games. *NeurIPS*.
- Oquab, M., Darcet, T., Moutakanni, T., Vo, H. V., Szafraniec, M., Khalidov, V., Fernandez, P., HAZIZA, D., Massa, F., El-Nouby, A., Assran, M., Ballas, N., Galuba, W., Howes, R., Huang, P.-Y., Li, S.-W., Misra, I., Rabbat, M., Sharma, V., Synnaeve, G., Xu, H., Jegou, H., Mairal, J., Labatut, P., Joulin, A., and Bojanowski, P. (2024). DINOv2: Learning robust visual features without supervision. *TMLR*.
- Radford, A., Kim, J. W., Hallacy, C., Ramesh, A., Goh, G., Agarwal, S., Sastry, G., Askell, A., Mishkin, P., Clark, J., Krueger, G., and Sutskever, I. (2021). Learning transferable visual models from natural language supervision. *ICML*.
- Robine, J., Höftmann, M., Uelwer, T., and Harmeling, S. (2023). Transformer-based world models are happy with 100k interactions. *ICLR*.
- Rubinstein, R. Y. (1997). Optimization of computer simulation models with rare events. *European Journal of Operational Research*.
- Sermanet, P., Lynch, C., Chebotar, Y., Hsu, J., Jang, E., Schaal, S., Levine, S., and Brain, G. (2018). Time-contrastive networks: Self-supervised learning from video. *ICRA*.
- Siméoni, O., Vo, H. V., Seitzer, M., Baldassarre, F., Oquab, M., Jose, C., Khalidov, V., Szafraniec, M., Yi, S., Ramamonjisoa, M., et al. (2025). Dinov3. *arXiv preprint arXiv:2508.10104*.
- Sobal, V., Zhang, W., Cho, K., Balestriero, R., Rudner, T. G. J., and LeCun, Y. (2025). Learning from reward-free offline data: A case for planning with latent dynamics models. *NeurIPS*.
- Sontag, E. D. (1998). *Mathematical Control Theory: Deterministic Finite Dimensional Systems*. Texts in Applied Mathematics. Springer, 2 edition.
- Sutton, R. S. (1991). Dyna, an integrated architecture for learning, planning, and reacting. *SIGART Bull.*
- Terver, B., Yang, T.-Y., Ponce, J., Bardes, A., and LeCun, Y. (2025). What drives success in physical planning with joint-embedding predictive world models? *arXiv preprint arXiv:2512.24497*.
- van den Oord, A., Vinyals, O., and Kavukcuoglu, K. (2017). Neural discrete representation learning.
- Watter, M., Springenberg, J. T., Boedecker, J., and Riedmiller, M. (2015). Embed to control: A locally linear latent dynamics model for control from raw images. *NeurIPS*.
- Williams, G., Aldrich, A., and Theodorou, E. (2015). Model predictive path integral control using covariance variable importance sampling. *arXiv preprint arXiv:1509.01149*.
- Yang, Y. and Ren, M. (2025). Memory storyboard: Leveraging temporal segmentation for streaming self-supervised learning from egocentric videos. *CoLLAs*.
- Zhang, M., Vikram, S., Smith, L., Abbeel, P., Johnson, M. J., and Levine, S. (2019). Solar: Deep structured representations for model-based reinforcement learning. *ICML*.

Zhou, G., Pan, H., LeCun, Y., and Pinto, L. (2025). Dino-wm: World models on pre-trained visual features enable zero-shot planning. *ICML*.

Zhu, J., Evtimova, K., Chen, Y., Shwartz-Ziv, R., and LeCun, Y. (2024). Variance-covariance regularization improves representation learning. *arXiv preprint arXiv 2306.13292*.

Appendix

A Environments

A.1 Wall

This is a 2D navigation environment introduced by [Zhou et al. \(2025\)](#) and [Sobal et al. \(2025\)](#). The environment consists of two rooms separated by a wall with a single narrow door. To move between rooms, the agent must pass through this door. The task is to navigate from a start position to a target position, given start and target images. The action space consists of 2D vectors representing displacements in x and y axes.

For training, we follow the approach of [Zhou et al. \(2025\)](#) to generate a dataset of 1,920 trajectories, each 50 time steps long. We train for 20 epochs.

A.2 PointMaze (UMaze and Medium-Maze)

This is a 2D navigation environment based on the MuJoCo physics engine ([Fu et al., 2020](#)). We experiment on the “UMaze” and “Medium-Maze” here and plan to test other maze setups in future work. The task is to navigate from a start position to a target position, given start and target images. Unlike the previous ‘Wall’ environment, the agent’s dynamics are governed by realistic physical properties such as velocity, acceleration, and inertia. The action space consists of forces applied along the x and y axes.

For training, we follow [Zhou et al. \(2025\)](#) to generate a dataset of 2,000 trajectories for UMaze and 4,000 for Medium-Maze, each 100 time steps long. We train for 20 epochs.

A.3 PushT

This is a challenging, contact-rich environment introduced by [Chi et al. \(2025\)](#). PushT features a pusher agent interacting with a T-shaped block. Starting from a random initial state, the agent must drive both the pusher and the T-block to a known feasible target configuration matching their target poses. The fixed green T is not the T-block’s target and is only a visual reference marker.

We use training data from [Zhou et al. \(2025\)](#), which contains 18500 trajectories with lengths of 100-300. We train for 2 epochs.

B Experiments

B.1 Model Predictive Control (MPC)

We outline the MPC algorithm below. Unlike DINO-WM (Zhou et al., 2025) that uses Cross-Entropy Method (CEM) as the subplanner, we use gradient descent instead to accelerate planning.

a) **Encode States:** Given the current observation o_0 and the goal observation o_g (both RGB images), we first encode them into their latent state representations using our trained encoder \mathcal{E}^s (either a pre-trained DINOv2 encoder plus a projector, or a ResNet from scratch):

$$z_0 = \mathcal{E}^s(o_0), \quad z_g = \mathcal{E}^s(o_g).$$

b) **Initialize Actions:** An initial action sequence for the planning horizon T is sampled from Gaussian distribution, $\{a_0, a_1, \dots, a_{T-1}\}$.

c) **Define Objective:** The planning objective is to minimize the mean squared error (MSE) between the predicted final latent state \hat{z}_T and the goal state z_g :

$$C = \|\hat{z}_T - z_g\|^2$$

where the latent trajectory is predicted by recursively applying the world model: $\hat{z}_t = f_\theta(\hat{z}_{t-1}, a_{t-1})$.

d) **Optimize via Gradient Descent:** Update actions iteratively using gradients of the cost with respect to the actions:

$$a_t \leftarrow a_t - \eta \frac{\partial C}{\partial a_t}, \quad \text{for } t = 0, \dots, T-1,$$

where η is the learning rate. Repeat until reaching the predefined number of iterations.

e) **Execute Action:** After the optimization loop is complete, the first k actions from the optimized action sequence are executed in the environment.

f) **Re-plan:** The process is repeated from step (a) at the next environment timestep, using the new observation o_1 .

B.2 Planning: GD v.s. CEM

We compare the open-loop success rate using GD and CEM planners. Here, we use 200 samples per iteration and 10 optimization steps for CEM. Similarly to what was observed in prior works (Zhou et al., 2025), CEM leads to better success rate, but we note that the planning time is significantly larger than GD. With straightening, the gap between GD and CEM planners is largely decreased. Our straightening regularization also consistently results in better performance with both planners.

Table 3: Goal-reaching Success Rate of 50 Test Samples (%) in open-loop planning. We compare GD and CEM planners. Values are mean \pm std over three data seeds. The best value is **bold.**

Method	Config		Wall		PointMaze – Umaze		PointMaze – Medium		PushT	
	dim	\mathcal{L}_{curv}	GD	CEM	GD	CEM	GD	CEM	GD	CEM
DINOv2 (patch)	14 × 14 × 384	✗	73.33 ± 3.40	87.33 ± 4.99	63.33 ± 8.22	88.00 ± 1.63	70.00 ± 4.08	88.00 ± 1.63	62.67 ± 4.11	71.33 ± 7.72
DINOv2 (patch) + proj	14 × 14 × 8	✗	80.00 ± 7.12	92.00 ± 0.00	44.00 ± 7.12	75.33 ± 4.99	72.00 ± 4.32	92.67 ± 4.71	70.00 ± 1.63	71.33 ± 6.18
DINOv2 (patch) + proj	14 × 14 × 8	✓	90.67 ± 0.94	100.00 ± 0.00	94.00 ± 1.63	94.00 ± 1.63	82.67 ± 3.77	86.67 ± 1.89	77.33 ± 6.18	80.00 ± 4.32
ResNet	14 × 14 × 8	✗	1.33 ± 1.89	1.33 ± 0.94	14.67 ± 4.99	20.67 ± 0.94	18.67 ± 4.11	24.00 ± 4.32	71.33 ± 7.36	56.00 ± 0.00
ResNet	14 × 14 × 8	✓	84.67 ± 2.49	90.00 ± 5.89	64.67 ± 8.38	83.33 ± 2.49	80.67 ± 0.94	89.33 ± 6.18	70.67 ± 0.94	72.67 ± 6.60

B.3 Hyperparameters

Table 4: Training Hyperparameters.

Name	Value
Projector/ResNet lr	$1e-5^a$
Predictor lr	$5e-4$
Action/Prop encoder lr	$5e-4$
Batch size	32
History frames	3
Frameskip	5

a. We observe severe performance degradation when training without straightening and decreasing the learning rate helps. We thus use $lr = 1e - 6$ for no straightening.

Table 5: Planning Hyperparameters.

Name	Value
Subplanner horizon	25
# Executed actions	25^a
Optimizer	Adam
Action Initialization	Zero
Learning rate	0.01
#opt steps	100

a. This is for open-loop. If using MPC, we execute the first 5 actions (or the first chunk of actions if using a frameskip of 5).

B.4 Effect of Feature Dimensions

In order to improve efficiency and efficacy, we ablate the output dimensions of the encoders. Here, we test on the “frozen DINOv2 + spatial projector” setup and preserve the spatial dimensions of the DINOv2 patch features $m_v = 196$ but decreasing channels from 384 to $d_v \in \{2, 8, 32, 128\}$. For all experiments, we use $lr = 1e - 6$ for the encoder. If with straightening, we apply straightening on the pooling head as described in Section B.5 with a straightening strength $\lambda = 0.1$.

We report the open-loop planning success rate of 50 test samples over three data sampling seeds in Figure 10. Very small dimensions (e.g., $d_v = 2$) result in poor performance, indicating insufficient capacity to preserve planning-relevant information. Increasing to a moderate dimension ($d_v = \{8, 32\}$) yields the best results, while too large dimensions ($d_v = 128$) consistently reduce success rates. This suggests that overly high-dimensional latents can hinder gradient-based planning.

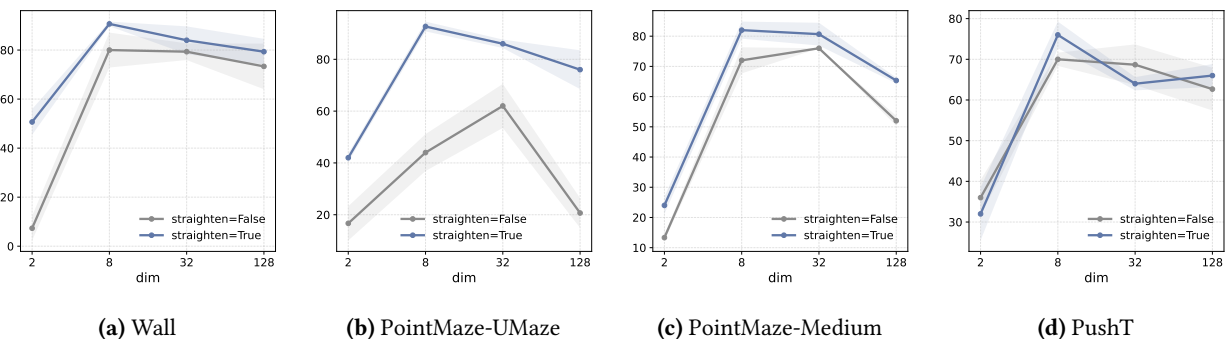


Figure 10: Comparison of Different Dimensions. The line plots show the success rate changes with increasing channels. Too small dimensions (e.g. $d_v = 2$) are unable to encode sufficient planning-relevant information, while unnecessarily high dimensions (e.g. $d_v = 128$) hinder the planning performance.

B.5 Cosine similarity variants for spatial features

For spatial visual features $z_t^v \in \mathbb{R}^{m_v \times d_v}$ ($m_v > 1$), we compute straightness from approximate latent velocities $v_t := z_{t+1}^v - z_t^v \in \mathbb{R}^{m_v \times d_v}$. Let $v_{t,i} \in \mathbb{R}^{d_v}$ denote the i -th patch vector and $\cos(u, w) = \frac{u^\top w}{\|u\|_2 \|w\|_2}$. We ablate four choices of \mathcal{C}_t :

- **[patch]** We treat each patch independently, then average:

$$\mathcal{C}_t = \frac{1}{m_v} \sum_{i=1}^{m_v} \cos(v_{t,i}, v_{t+1,i}).$$

- **[mean]** We average patches to one vector, then cosine:

$$\bar{v}_t = \frac{1}{m_v} \sum_{i=1}^{m_v} v_{t,i}, \quad \mathcal{C}_t = \cos(\bar{v}_t, \bar{v}_{t+1}).$$

- **[flatten]** We flatten the spatial features and single cosine over all dimensions:

$$\mathcal{C}_t = \cos(\text{vec}(v_t), \text{vec}(v_{t+1})),$$

where $\text{vec}(\cdot) : \mathbb{R}^{m_v \times d_v} \rightarrow \mathbb{R}^{m_v d_v}$.

- **[agg]** We learn a pooling head to aggregate features to a single global feature before cosine:

$$\mathcal{C}_t = \cos(h_\phi(v_t), h_\phi(v_{t+1})),$$

with a pooling head $h_\phi : \mathbb{R}^{m_v \times d_v} \rightarrow \mathbb{R}^{d_h}$. Concretely, we use an MLP with an output dimension of 128 as h_ϕ in all experiments.

We test these variants on the “frozen DINOv2 + spatial projector” setup and report the open-loop planning success rate of 50 test samples over three data sampling seeds in Figure 11. The projector projects pretrained DINOv2 patch features $e_t \in \mathbb{R}^{196 \times 384}$ to $z_t \in \mathbb{R}^{196 \times 8}$. For the straightening strength coefficient, we use $\lambda = 0.1$ for agg and $\lambda = 0.01$ for the rest, as these values yield the best performance. We find that using a learnable pooling head performs best. This is not surprising as straightening should act on the *global* trajectory representations, whereas spatial tokens mainly capture local, patch-level variations that are only loosely aligned across time due to object motion and occlusion.

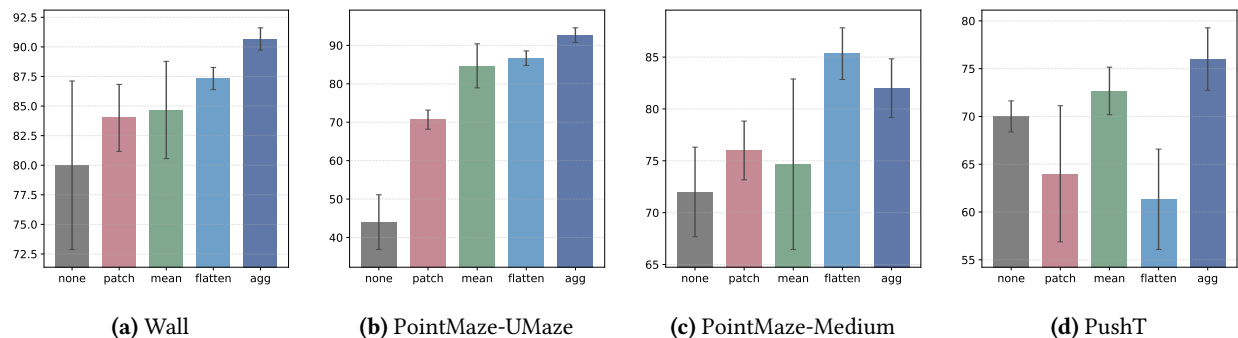


Figure 11: Comparison of Different Straightening Strategies. The bar charts show the planning success rates. While all cosine similarity variants lead to better performance than no straightening, adding a learnable pooling head gives the best performance.

C Theoretical Analysis

C.1 Setup and notation

We optimize an action sequence $\mathbf{a} = (a_0, \dots, a_{K-1}) \in \mathbb{R}^{K \times d_a}$ over horizon K to minimize the terminal MSE

$$\mathcal{L}(\mathbf{a}) = \|z_K - z_g\|_2^2, \quad z_K = \Phi(\mathbf{a}), \quad (14)$$

where Φ denotes unrolling the latent dynamics from a fixed initial state z_0 .

Assumption C.1 (Linear latent dynamics). *We assume linear latent dynamics*

$$z_{t+1} = Az_t + Ba_t, \quad A \in \mathbb{R}^{d \times d}, B \in \mathbb{R}^{d \times d_a}. \quad (15)$$

Definition C.2 (Effective condition number). For a PSD matrix $H \succeq 0$ with a nontrivial nullspace, define

$$\kappa_{\text{eff}}(H) := \frac{\sigma_{\max}(H)}{\sigma_{\min}^+(H)},$$

where $\sigma_{\min}^+(H)$ is the smallest nonzero singular value.

Definition C.3 (ε -straight transition). In the linear model (15), define

$$\varepsilon := \|A - I\|_2.$$

C.2 Conditioning of the planning Hessian

Unrolling (15) gives the affine terminal map

$$z_K = A^K z_0 + \sum_{t=0}^{K-1} A^{K-1-t} B a_t. \quad (16)$$

Define the rollout Jacobian

$$J_\Phi := \frac{\partial z_K}{\partial \mathbf{a}} = [A^{K-1}B \quad A^{K-2}B \quad \dots \quad B] \in \mathbb{R}^{d \times (Kd_a)}. \quad (17)$$

The associated finite-horizon discrete controllability Gramian is

$$\mathcal{W}_K := J_\Phi J_\Phi^\top = \sum_{k=0}^{K-1} A^k B B^\top (A^\top)^k \in \mathbb{R}^{d \times d}, \quad (18)$$

a standard term in linear systems (Kailath, 1980; Sontag, 1998; Chen, 1999).

Lemma C.4 (Hessian form and Gramian equivalence). *Under (14)–(15), the planning Hessian satisfies*

$$H := \nabla_{\mathbf{a}}^2 \mathcal{L}(\mathbf{a}) = 2J_\Phi^\top J_\Phi \succeq 0. \quad (19)$$

Moreover, the nonzero singular values of $J_\Phi^\top J_\Phi$ equal those of $J_\Phi J_\Phi^\top$, hence

$$\kappa_{\text{eff}}(H) = \kappa(\mathcal{W}_K). \quad (20)$$

Proof. H is positive semi-definite by definition.

Since z_K is affine in \mathbf{a} by (16), $\mathcal{L}(\mathbf{a}) = \|z_K - z_g\|_2^2$ is a convex quadratic, and direct differentiation yields $H = 2J_\Phi^\top J_\Phi \succeq 0$. For any matrix M , the nonzero eigenvalues of $M^\top M$ and MM^\top coincide. Applying this with $M = J_\Phi$ gives that the nonzero eigenvalues of $H/2$ equal those of \mathcal{W}_K , which implies (20). ■

Theorem C.5 (Conditioning bound). *Assume (15). Consider first the square-action case $d_a = d$ with B invertible. Then*

$$\kappa_{\text{eff}}(H) = \kappa(\mathcal{W}_K) \leq \kappa(B)^2 \frac{\sum_{k=0}^{K-1} \sigma_{\max}(A)^{2k}}{\sum_{k=0}^{K-1} \sigma_{\min}(A)^{2k}} \leq \kappa(B)^2 \kappa(A)^{2(K-1)}, \quad (21)$$

where $\kappa(A) := \sigma_{\max}(A)/\sigma_{\min}(A)$. If additionally $\varepsilon = \|A - I\|_2 < 1$, then

$$\kappa_{\text{eff}}(H) \leq \kappa(B)^2 \left(\frac{1 + \varepsilon}{1 - \varepsilon} \right)^{2(K-1)} \leq \kappa(B)^2 e^{6\varepsilon K} \quad (\varepsilon \leq \frac{1}{2}). \quad (22)$$

Proof. By Lemma C.4, it suffices to bound $\kappa(\mathcal{W}_K)$.

Upper bound. For any unit vector $x \in \mathbb{R}^d$,

$$x^\top \mathcal{W}_K x = \sum_{k=0}^{K-1} \|B^\top (A^\top)^k x\|_2^2 \leq \sum_{k=0}^{K-1} \|B\|_2^2 \|A^k\|_2^2 \|x\|_2^2 \leq \sigma_{\max}(B)^2 \sum_{k=0}^{K-1} \sigma_{\max}(A)^{2k}.$$

Taking the maximum over $\|x\|_2 = 1$ yields

$$\lambda_{\max}(\mathcal{W}_K) \leq \sigma_{\max}(B)^2 \sum_{k=0}^{K-1} \sigma_{\max}(A)^{2k}.$$

Lower bound. Since B is invertible, $\|B^\top u\|_2 \geq \sigma_{\min}(B) \|u\|_2$ for all u . Also $\sigma_{\min}(A^k) \geq \sigma_{\min}(A)^k$. Thus for any unit x ,

$$\|B^\top (A^\top)^k x\|_2 \geq \sigma_{\min}(B) \|(A^\top)^k x\|_2 \geq \sigma_{\min}(B) \sigma_{\min}(A^k) \|x\|_2 \geq \sigma_{\min}(B) \sigma_{\min}(A)^k,$$

hence

$$x^\top \mathcal{W}_K x \geq \sigma_{\min}(B)^2 \sum_{k=0}^{K-1} \sigma_{\min}(A)^{2k}.$$

Taking the minimum over $\|x\|_2 = 1$ yields

$$\lambda_{\min}(\mathcal{W}_K) \geq \sigma_{\min}(B)^2 \sum_{k=0}^{K-1} \sigma_{\min}(A)^{2k}.$$

Combine. Dividing the two bounds gives the first inequality in (21). For the second, use positivity of terms:

$$\frac{\sum_{k=0}^{K-1} \sigma_{\max}(A)^{2k}}{\sum_{k=0}^{K-1} \sigma_{\min}(A)^{2k}} \leq \max_{0 \leq k \leq K-1} \frac{\sigma_{\max}(A)^{2k}}{\sigma_{\min}(A)^{2k}} = \kappa(A)^{2(K-1)}.$$

ε -specialization. If $\varepsilon = \|A - I\|_2 < 1$, then by Weyl's perturbation theorem, $\sigma_{\max}(A) \leq 1 + \varepsilon$ and $\sigma_{\min}(A) \geq 1 - \varepsilon$, which implies the first inequality in (22). For $\varepsilon \leq \frac{1}{2}$, the standard bound $\ln\left(\frac{1+\varepsilon}{1-\varepsilon}\right) \leq 3\varepsilon$ gives the exponential form. ■

Remark C.6 (Low-dimensional actions $d_a < d$). If $d_a < d$, then B is not invertible and \mathcal{W}_K may be singular. All statements hold on the controllable subspace $\mathcal{S}_K = \text{range}(\mathcal{W}_K)$ by replacing $\lambda_{\min}(\mathcal{W}_K)$ with $\lambda_{\min}^+(\mathcal{W}_K)$ and interpreting $\kappa(\mathcal{W}_K)$ as an effective condition number. In this case, additional controllability assumptions are needed to lower bound $\sigma_{\min}^+(\mathcal{W}_K)$.

C.3 Cosine similarity as a proxy

Assumption C.7 (Constant velocity and smooth actions). Define latent velocities $v_t := z_{t+1} - z_t$. Assume there exists a constant $c > 0$ such that

$$\|v_t\|_2 = c \quad \text{for all } t = 0, \dots, K-1.$$

Assume action smoothness $\Delta_a := \max_t \|a_{t+1} - a_t\|_2 < \infty$.

Definition C.8 (Cosine similarity). For $t = 0, \dots, K-2$, define

$$\mathcal{C}_t := \cos(v_t, v_{t+1}) = \frac{v_t^\top v_{t+1}}{\|v_t\|_2 \|v_{t+1}\|_2}, \quad \bar{\mathcal{C}} := \frac{1}{K-1} \sum_{t=0}^{K-2} \mathcal{C}_t.$$

Proposition C.9 (Cosine proxy \Rightarrow small $(A-I)$ along visited directions). Under linear dynamics (15), let $\hat{v}_t := v_t / \|v_t\|_2$. Under Assumption C.7, for each $t = 0, \dots, K-2$,

$$\|(A-I)\hat{v}_t\|_2 \leq \sqrt{2(1-\mathcal{C}_t)} + \frac{\sigma_{\max}(B)\Delta_a}{c}. \quad (23)$$

If $\bar{\mathcal{C}} \geq 1 - \eta$, then

$$\frac{1}{K-1} \sum_{t=0}^{K-2} \|(A-I)\hat{v}_t\|_2 \leq \sqrt{2\eta} + \frac{\sigma_{\max}(B)\Delta_a}{c}. \quad (24)$$

Proof. Under (15),

$$v_{t+1} - v_t = (z_{t+2} - z_{t+1}) - (z_{t+1} - z_t) = (A-I)(z_{t+1} - z_t) + B(a_{t+1} - a_t) = (A-I)v_t + B(a_{t+1} - a_t).$$

Thus, by the triangle inequality,

$$\|(A-I)\hat{v}_t\|_2 = \frac{\|(A-I)v_t\|_2}{\|v_t\|_2} \leq \frac{\|v_{t+1} - v_t\|_2}{\|v_t\|_2} + \frac{\|B(a_{t+1} - a_t)\|_2}{\|v_t\|_2} \leq \frac{\|v_{t+1} - v_t\|_2}{c} + \frac{\sigma_{\max}(B)\Delta_a}{c}.$$

Since $\|v_t\|_2 = \|v_{t+1}\|_2 = c$,

$$\|v_{t+1} - v_t\|_2^2 = \|v_{t+1}\|_2^2 + \|v_t\|_2^2 - 2v_{t+1}^\top v_t = 2c^2(1 - \mathcal{C}_t),$$

hence $\|v_{t+1} - v_t\|_2/c = \sqrt{2(1-\mathcal{C}_t)}$, proving (23). Averaging and applying Jensen's inequality to the concave map $x \mapsto \sqrt{x}$ gives

$$\frac{1}{K-1} \sum_{t=0}^{K-2} \sqrt{1-\mathcal{C}_t} \leq \sqrt{1-\bar{\mathcal{C}}} \leq \sqrt{\eta},$$

which implies (24). ■

Remark C.10 (Directional vs. spectral control). Proposition C.9 bounds $(A-I)$ only along visited directions $\{\hat{v}_t\}$. Upgrading this to a uniform spectral bound $\varepsilon = \|A-I\|_2$ requires an additional coverage condition so that visited directions span the latent space. This is not an impractical assumption since training trajectories are typically collected to be diverse. Under such regimes, maximizing cosine similarity provides a meaningful proxy for making A close to I in spectral norm.

D Visualizations

D.1 Distance Heatmaps

We plot heatmaps of the Euclidean distances in the embedding space. The yellow star represents the target, and we compute the Euclidean distance between its embedding and those of all other states in the maze. Blue indicates small values, and red indicates large values. With straightening, the latent distance accurately reflects the minimum number of steps required to reach the target.

To compare the distance heatmaps, we compare with ground-truth heatmaps constructed by dividing the mazes into discrete grids and applying the A-star algorithm. 4-neighbor connectivity means each grid cell connects only to up/down/left/right cells. 8-neighbor connectivity adds the four diagonals (up-left, up-right, down-left, down-right), so paths can cut corners diagonally and distances are usually shorter.

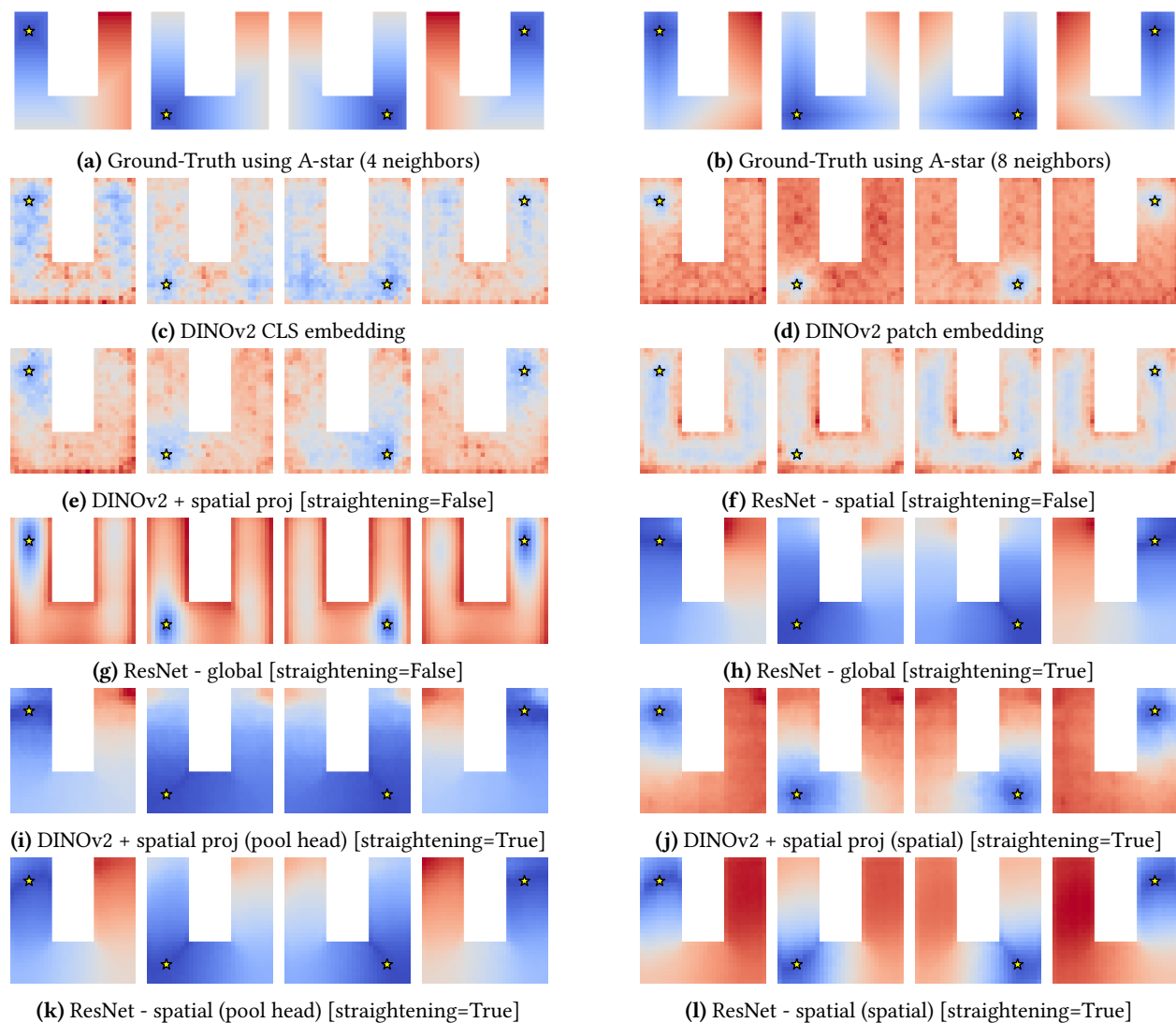


Figure 12: Distance heatmaps of PointMaze-UMaze.

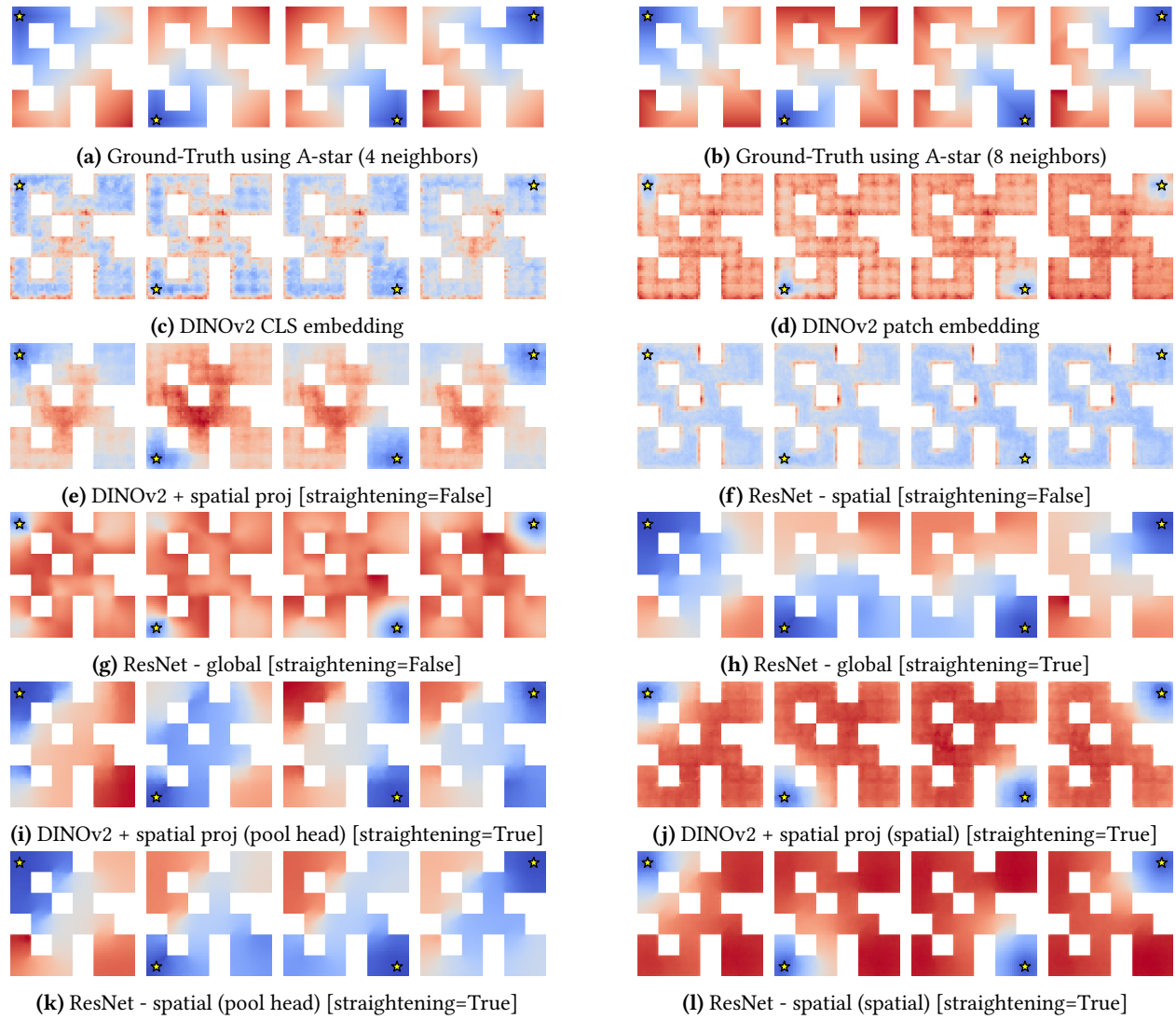


Figure 13: Distance heatmaps of *PointMaze-Medium*.

D.2 Visualization of Latent Trajectories

To visualize the learned representations of the trajectories, we randomly sample trajectories with a length of 30 and plot them in 2D using PCA. Here, we use DINO CLS token embeddings and the pooled features of our model (trained with straightening). While latent trajectories are highly curved in DINO CLS embedding space, they become significantly smoother after straightening. Additionally, we compute the MSE between the embeddings of each intermediate state and the target. The Euclidean distance is closer to the geodesic distance for straighter trajectories, and thus MSE (which is squared Euclidean distance) becomes a more useful planning cost function that can reflect the true progress towards the target. Visualizations for different environments are in Figures 14 to 17.

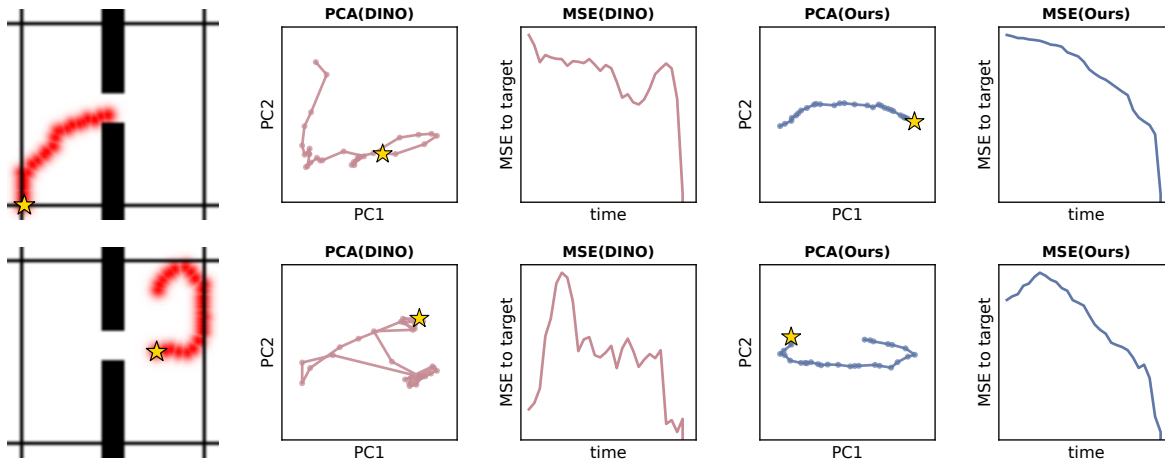


Figure 14: PCA of Trajectories of Wall.

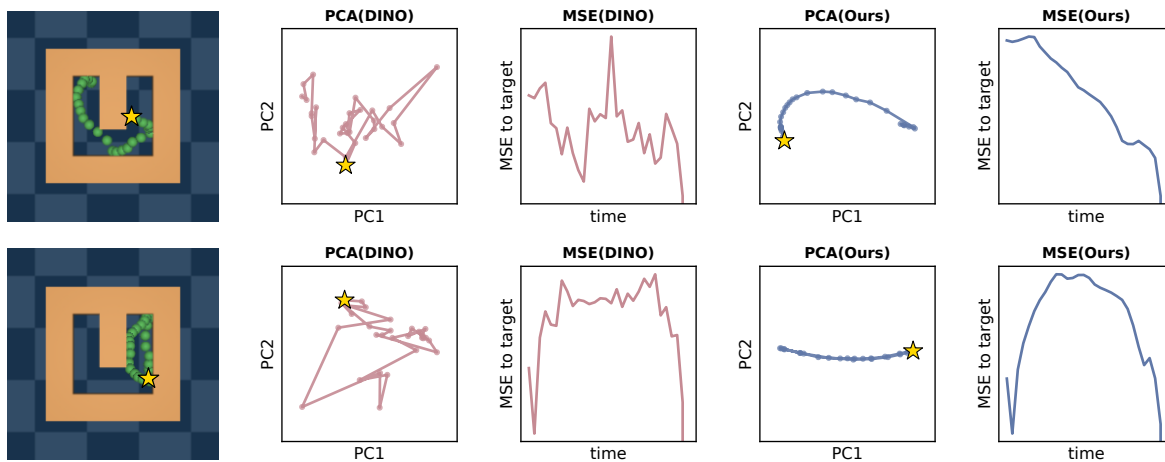


Figure 15: PCA of Trajectories of PointMaze-UMaze.

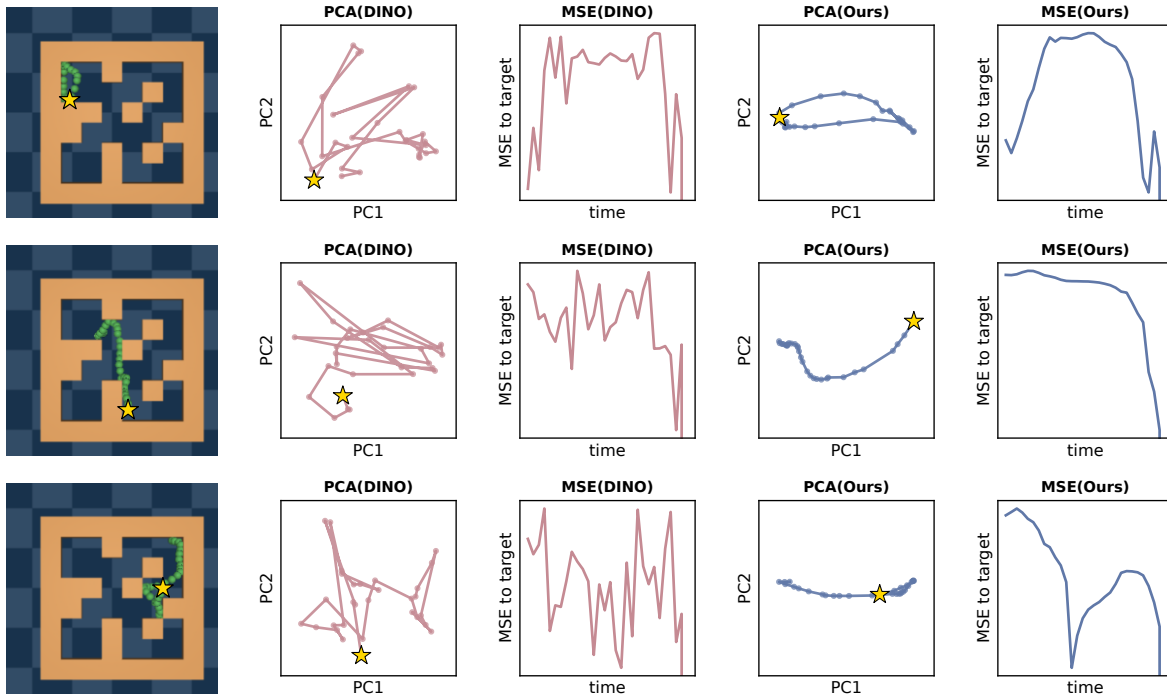


Figure 16: PCA of Trajectories of PointMaze-Medium.

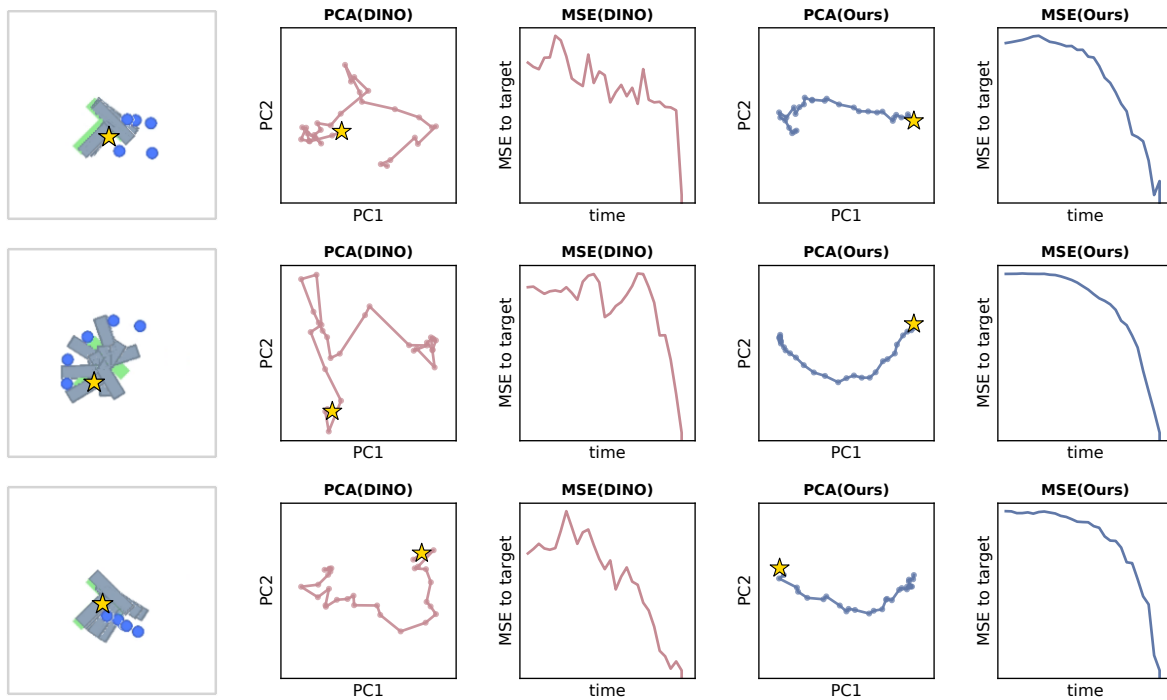


Figure 17: PCA of Trajectories of PushT. The overlaid figures only include five samples for readability.

D.3 Planning Trajectories

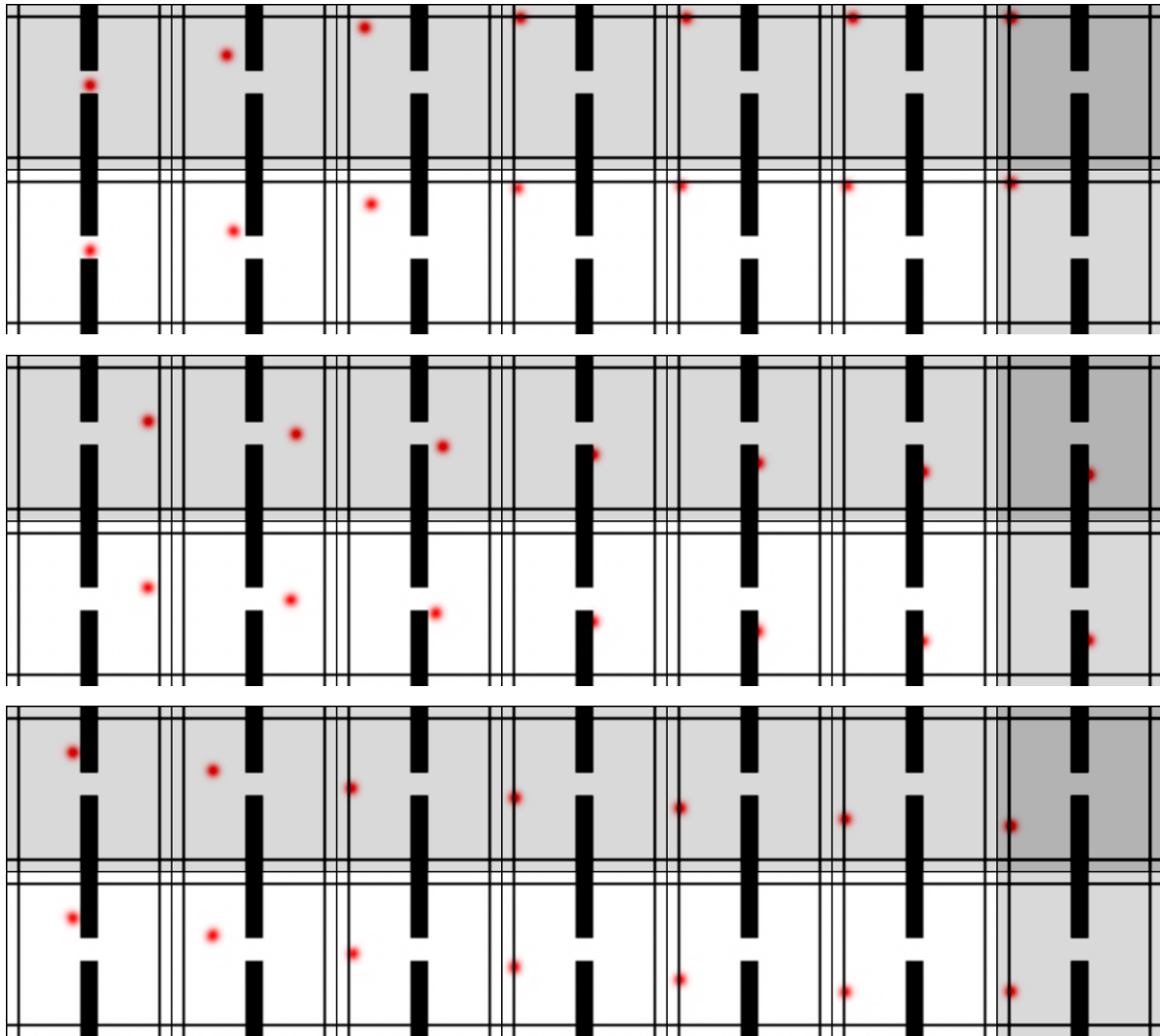


Figure 18: *Open-Loop Planning Trajectories of Wall. The first row is from the simulator and the second from the decoder.*



Figure 19: *Open-Loop Planning Trajectories of PointMaze-UMaze. The first row is from the simulator and the second from the decoder.*

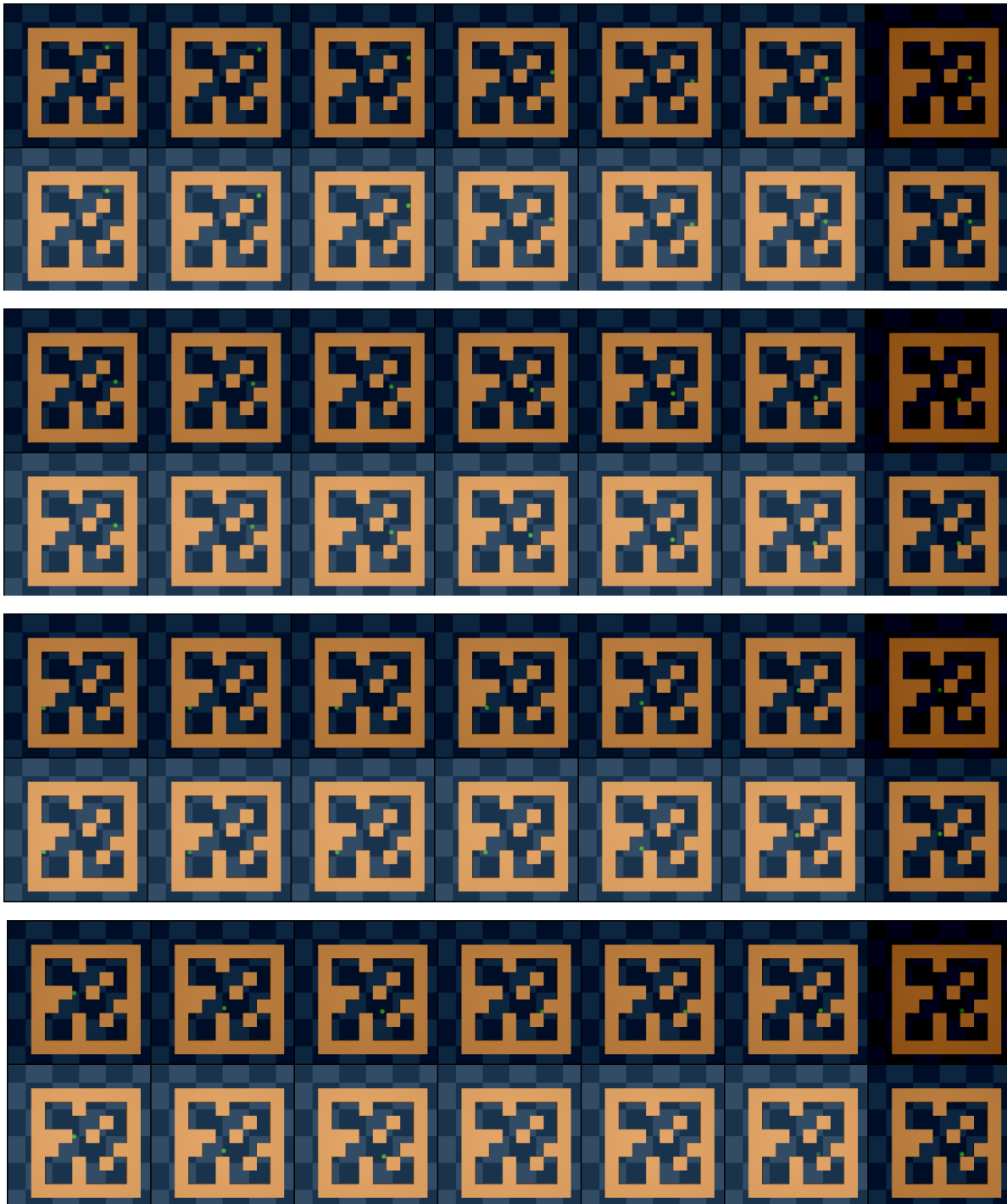


Figure 20: Open-Loop Planning Trajectories of *PointMaze-Medium*. The first row is from the simulator and the second from the decoder.

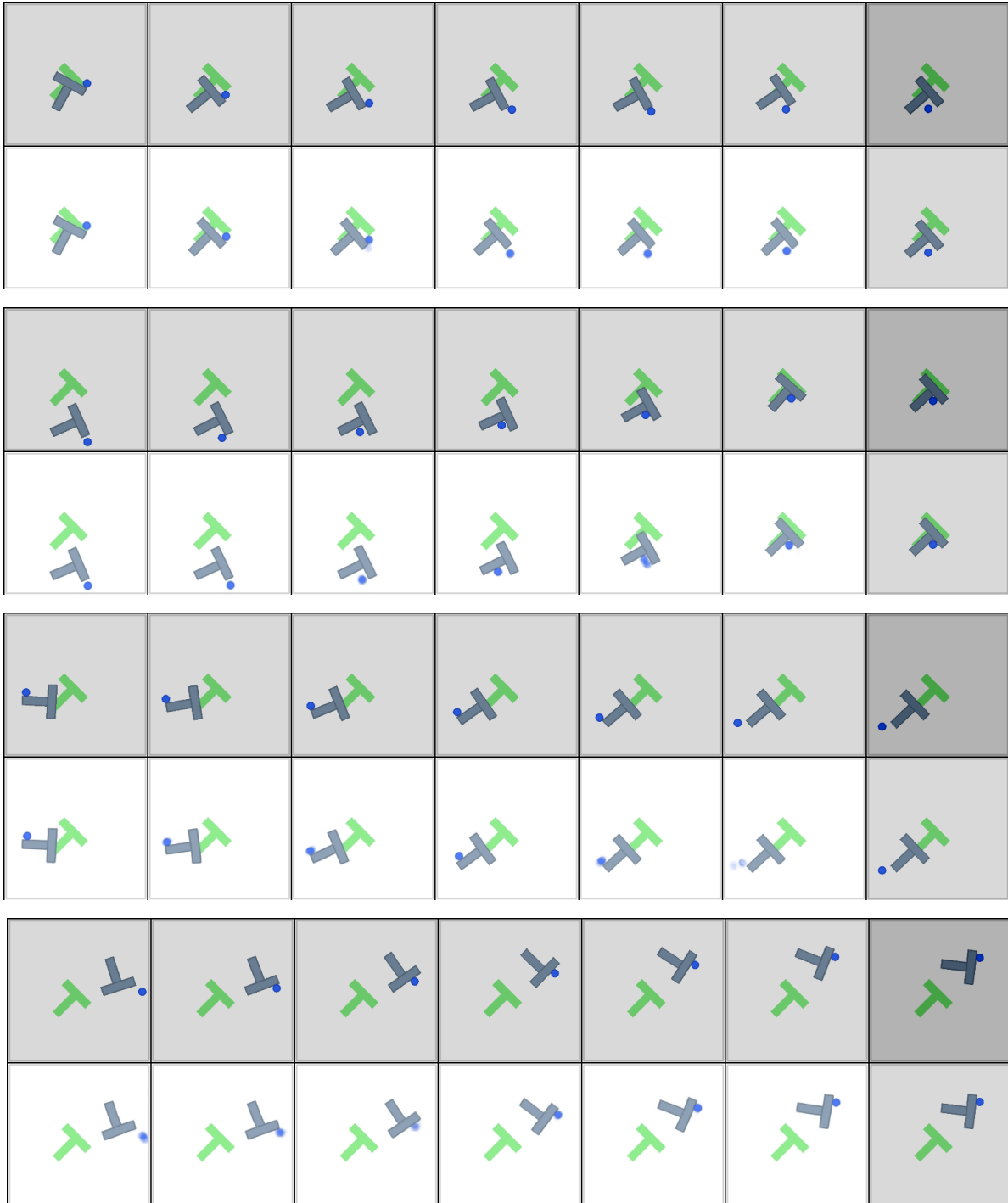


Figure 21: *Open-Loop Planning Trajectories of PushT. The first row is from the simulator and the second from the decoder.*

E Teleported PointMaze

This is a novel 2D navigation environment adapted from PointMaze. The core modification is a one-way teleportation dynamic. While the top, bottom, and left boundaries of the maze function as standard solid obstacles, a predefined region near the right wall acts as a teleportation trigger. If an agent’s state transition at time t results in a new x-position x_{t+1} that crosses this threshold (i.e., $x_{t+1} > x_{\text{right-border}}$), an instantaneous state intervention occurs, modifying the agent’s state as follows:

1. Position (x): The agent’s x-position is reset to the left side of the maze: $x_{t+1} \leftarrow x_{\text{left-border}}$.
2. Position (y): The agent’s y-position y_{t+1} is preserved.
3. Velocity (x): The agent’s x-axis velocity v_x is reset to its absolute value: $v_{x,t+1} \leftarrow |v_{x,t}|$.

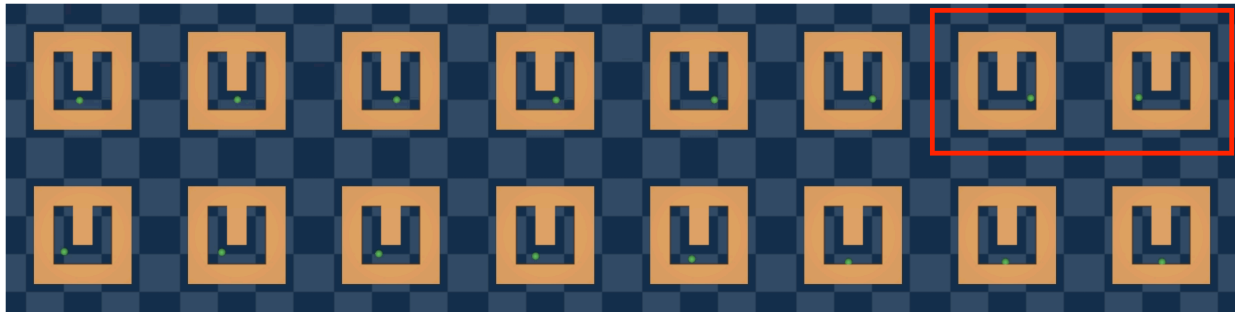


Figure 22: Teleported PointMaze. Note that the teleportation happens within the red box.

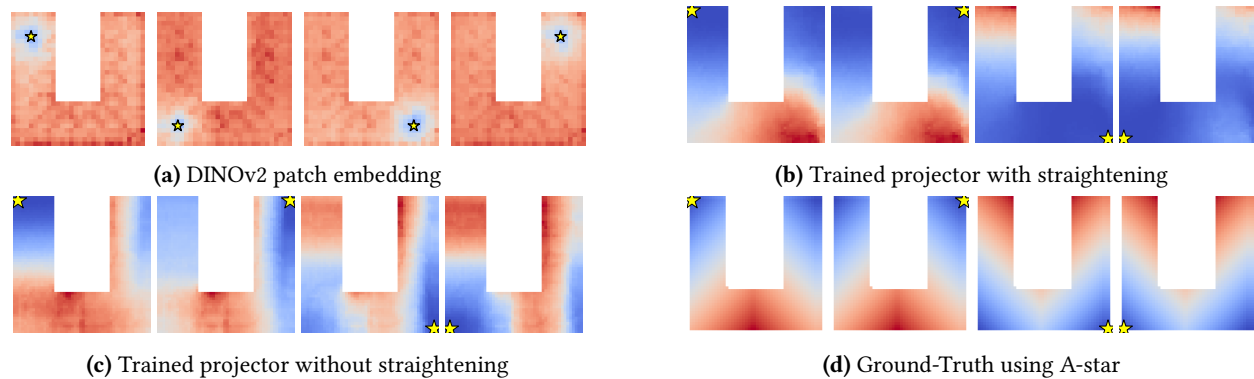
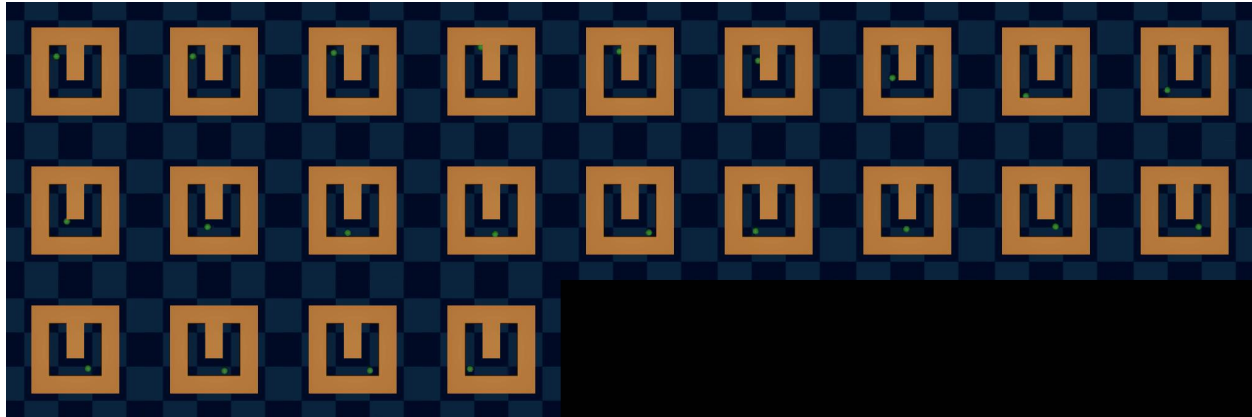
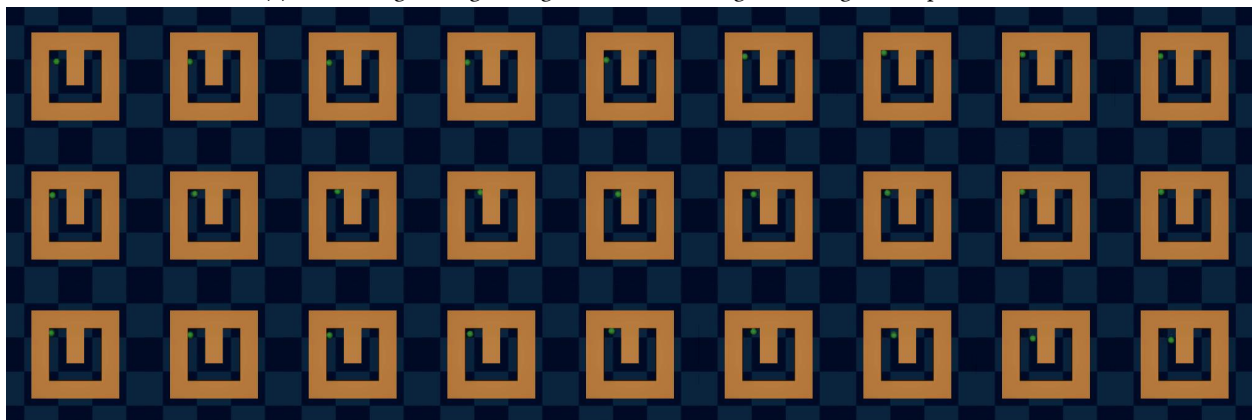


Figure 23: Distance heatmaps of Teleport-PointMaze (blue indicates small values, red indicates large values). The state marked by the yellow star is used as the target, and we compute the MSE between its embedding and those of all other states in the maze. With straightening, the resulting heatmaps are significantly closer to the ones obtained using A-star.



(a) With straightening, the agent reaches the target within given step limit.



(b) Without straightening, the agent gets stuck at the corner.

Figure 24: Comparison of Planning Trajectories in Teleport-PointMaze. The frames were masked by black after reaching the target.